A Moist PBL Parameterization for Large-Scale Models and Its Application to Subtropical Cloud-Topped Marine Boundary Layers

HERVÉ GRENIER AND CHRISTOPHER S. BRETHERTON

Department of Atmospheric Sciences, University of Washington, Seattle, Washington

(Manuscript received 10 January 2000, in final form 19 July 2000)

ABSTRACT

A new general purpose boundary layer parameterization that permits realistic treatment of stratocumulus-capped boundary layers (SCBLs) with coarse vertical resolution is described. It combines a 1.5-order turbulent closure model with an entrainment closure at the boundary layer top. Three different implementations of the entrainment closure, in which the boundary layer height is respectively prognosed, reconstructed from thermodynamic values at the grid points, or restricted to lie on a flux level of the host model grid, are tested in a single-column modeling framework at both fine and coarse vertical resolution. The first two approaches permit a stratocumulus top and base to lie between grid levels and evolve continuously with time, but are more complicated to implement in a three-dimensional model.

The model performs very well in cases of dry convection, whatever the inversion implementation and the vertical resolution. With 15-mb or better vertical resolution, all approaches properly simulate mixing in SCBLs, including daytime cloud thinning and a transition to decoupling and conditional instability as SST increases. With coarser resolution, details of the implementation influence the simulated cloud thickness, which is systematically underestimated with the restricted inversion approach. A method for computing vertical advective fluxes at the boundary layer top that explicitly accounts for the inversion is presented; an essential component of the reconstructed inversion implementation, this vertical advection scheme also improves SCBL simulation at low resolution with a restricted inversion. For comprehensive simulation of boundary layer convection, this scheme should be coupled with a parameterization of shallow cumulus convection; this will be described in a forthcoming paper.

1. Introduction

In most global forecast models and general circulation models (GCMs), the cloud cover and boundary layer structure are not well represented in regions of persistent marine stratocumulus, particularly in the subtropics. Over the past 15 yr, field experiments and fine-scale numerical models have given us a reasonable understanding of stratocumulus-capped boundary layers (SCBLs). They suggest that a successful parameterization of the SCBL must (a) faithfully represent the tight coupling between cloud formation, convective turbulence, microphysical, radiative and surface fluxes, and (b) handle the internal stratification or ''decoupling'' of an SCBL that can be driven by some combination of high surface latent heat fluxes, daytime absorption of insolation within clouds, and drizzle. Criterion a allows for the formation and maintenance of a SCBL, while criterion b allows for the formation of cumulus under the main stratocumulus layer, which is often an important intermediary in the thinning and breakup of subtropical stratocumulus.

Almost no GCM parameterization used today satisfies both these criteria. Many GCMs assume unsaturated thermodynamics in their turbulence schemes. In many SCBLs, however, the dominant source of turbulent kinetic energy is buoyancy fluxes within the cloud layer. SCBLs in such models must be maintained unphysically by a mixture of dry convection and shallow cumulus convection. Bougeault (1985), Bechtold et al. (1995), and others have shown that 1.5 and higher order turbulence closure models (TCMs) can represent the dynamics and internal stratification of SCBLs quite well if they are formulated using moist thermodynamics and if the vertical grid resolution is 100 m or less. At coarser vertical resolution, this method breaks down (Bechtold et al. 1996) due to underresolution of the inversion and the cloud-layer structure.

In sections 2 and 3 of this paper, we describe a general purpose boundary layer parameterization that can simulate the boundary layer structure and cloud properties in SCBLs even at GCM vertical resolution. A 1.5-order TCM based on thermodynamic variables conserved for moist reversible adiabatic processes is used for the in-

Corresponding author address: Hervé Grenier, Dept. of Atmospheric Sciences, University of Washington, Box 351640, Seattle, WA 98195.
E-mail: herve@atmos.washington.edu

ternal structure of the boundary layer. In neutral to unstable conditions, an entrainment parameterization, rather than the TCM, is used to specify the vertical fluxes of heat, moisture, and momentum at the boundary layer top. An approach similar in spirit (insofar as it combined an internally varying boundary layer with an entrainment parameterization) was proposed many years ago by Randall (1976) in his pioneering doctoral thesis and was used for five years in the University of California, Los Angeles (UCLA) GCM. At the time, his state-of-the-art GCM had only nine levels for the entire atmosphere, which is perhaps too coarse for this type of approach. This approach was superceded in the UCLA GCM by a parameterization in which the planetary boundary layer (PBL) was taken to be a mixed layer whose top evolves according to an entrainment closure, and forms the bottom sigma level of the rest of the GCM (Suarez et al. 1983; Randall et al. 1985). This approach can elegantly represent entraining cloud-topped mixed layers, but does not attempt to resolve the internal structure of the PBL, and therefore cannot easily handle boundary layer decoupling or stable boundary layers. A PBL parameterization of this type, but with four layers internal to the PBL, is currently under development by the UCLA GCM group (A. Arakawa 2000, personal communication). Beljaars and Viterbo (1998) combined a nonlocal mixing scheme for dry convective boundary layers with an entrainment closure with good results; this approach is now implemented in the European Center for Medium-Range Weather Forecasts forecast model. Lock et al. (2000) have recently implemented a scheme coupling an entrainment parameterization to a nonlocal parameterization of moist PBL convection in the 40-layer U.K. Meteor. Office GCM, with encouraging results. Our approach is the first to couple a TCM to an entrainment parameterization.

Regardless of the PBL mixing and entrainment parameterizations used, important implementation issues arise that have not been adequately treated in the litterature. The first is how to represent the entrainment interface given a discrete vertical grid. In section 4, three implementations of the entrainment interface ere compared in a single-column modeling framework at both coarse and fine vertical resolution. In the ''prognostic inversion'' approach, the PBL depth is a prognostic variable, in the ''reconstructed inversion'' approach, the PBL height and the capping inversion strength are reconstructed from thermodynamic values at the grid points, and in the ''restricted inversion'' approach, the PBL height is restricted to lie on a flux level of the host model grid. The first two approaches permit a stratocumulus top and base to lie between grid levels and evolve continuously with time, but are more complicated to implement in a three-dimensional model. A continuously varying cloud thickness is desirable for the simulation of stratocumulus clouds, so that cloud microphysics and cloud feedbacks on turbulence and radiation are captured despite the coarseness of the grid.

The second implementation issue is how to ensure that radiation, vertical advection, and (if present) cumulus convection are handled by the host GCM consistently with the inversion representation in the PBL parameterization. Regarding radiation, Stevens et al. (1999) show how large eddy simulations (LES) of entrainment rate into radiatively driven boundary layers can be affected by underresolution of the radiative cooling zone (see their appendix C). Lenderink and Holtslag (2000) showed how poor performance of a classical TCM at low resolution, in which the inversion top gets unrealistically locked to a fixed grid level, can arise due to feedbacks between vertical advection of a poorly resolved inversion and turbulent mixing. In section 5, we propose a simple method to treat vertical advection consistently with the presence of an inversion, which we use with the profile reconstruction and restricted inversion approach.

To determine some parameters of the scheme, demonstrate its general performance at both high and low vertical resolution, and to compare the three possible inversion implementations, we present simulations of a dry convective boundary layer (section 6) and a stratocumulus to trade-cumulus transition (section 7). In these simulations, we have coupled the TCM to our own ''host single-column model'' consisting of cloud, radiation, surface fluxes, and vertical advection parameterizations. For simplicity, precipitation and shallow convection have not been included.

2. Turbulence closure model formulation

The prognostic variables are the two components u and v of the horizontal wind velocity, and two thermodynamic variables that are approximately conserved for moist reversible adiabatic processes. These are the linearized versions of the liquid water potential temperature θ_l (Betts 1973) and the total water mixing ratio q_t,

$$\theta_l = \theta - \frac{L}{C_p \Pi} q_l, \quad \text{and} \tag{1}$$

$$q_t = q_v + q_l. \tag{2}$$

Here and elsewhere, conventional notation is used where possible. The Exner function $\Pi = (p_{\text{ref}}/p)^{R_d/C_p}$. The sources/sinks for these variables are large-scale advection and the divergence of the convective turbulent fluxes, the radiative flux F_r, and the precipitation flux F_P.

Let D_h denote a time-derivative operator following the horizontal motion. We vertically discretize using a staggered grid with indices increasing with height. The basic prognostic variables are carried at the integer-indexed levels j, and their fluxes are carried at the intermediate levels $j + \frac{1}{2}$. The vertical difference operator $\delta^j X$ is defined as $X^{j+1/2} - X^{j-1/2}$. The pressure thicknesses of the thermodynamic layers are $\delta^j p$ and the dis-

tances between grid points are $\delta^{j+1/2}p$. We define the total energy flux

$$E = C_p \Pi \rho \overline{w'\theta_l'} + F_r, \tag{3}$$

and the total water flux

$$W = \rho \overline{w'q_t'} + F_P. \tag{4}$$

Overbars indicate ensemble averaged quantities and primes indicate deviations from the ensemble average over the grid cell. Bars over prognostic variables are dropped for clarity. With this notation, the vertically discretized budget equations for the prognostic variables are

$$\frac{D_h\theta_l^j}{Dt} = \frac{g}{C_p\Pi^j}\frac{\delta^j E}{\delta^j p} - \left(\overline{\omega}\frac{\partial\theta_l}{\partial p}\right)^j, \tag{5}$$

$$\frac{D_h q_t^j}{Dt} = g\frac{\delta^j W}{\delta^j p} - \left(\overline{\omega}\frac{\partial q_t}{\partial p}\right)^j, \tag{6}$$

$$\frac{D_h u^j}{Dt} = g\frac{\delta^j \overline{\rho w'u'}}{\partial^j p} + f(v^j - V_g^j) - \left(\overline{\omega}\frac{\partial u}{\partial p}\right)^j, \quad \text{and} \tag{7}$$

$$\frac{D_h v^j}{\partial t} = g\frac{\delta^j \overline{\rho w'v'}}{\delta^j p} - f(u^j - U_g^j) - \left(\overline{\omega}\frac{\partial v}{\partial p}\right)^j, \tag{8}$$

where U_g and V_g are the horizontal components of the geostrophic wind and $\overline{\omega}$ is the mean vertical velocity. In a GCM setting, both vertical and horizontal advection would be done by the host model. In a single-column model, horizontal advective tendencies are specified. Vertical advection is done as presented in section 5. For simplicity, we have used forward Euler time differencing, except for diffusive terms (the turbulent transports), for which we use a modified implicit (backward Euler) approach for stability. The method can easily be adapted to other time-differencing schemes.

a. Turbulent fluxes

The turbulent fluxes of θ_l, q_t, and momentum within the PBL are computed using an eddy diffusivity K_h for the conserved thermodynamic variables and an eddy viscosity K_m for the horizontal velocity components, both derived from the 1.5-order turbulence closure:

$$\overline{w'X'_{h,m}}^{j+1/2} = K_{h,m}^{j+1/2}\rho^{j+1/2}g\frac{\delta^{j+1/2}X}{\delta^{j+1/2}p}. \tag{9}$$

Following Mellor and Yamada (1982, hereafter MY82), K_h and K_m are related to the turbulent kinetic energy (TKE) $e^{j+1/2}$, a master turbulent master length scale ($l^{j+1/2}$), and stability functions $S_h^{j+1/2}$ and $S_m^{j+1/2}$ as

$$K_{h,m}^{j+1/2} = l^{j+1/2}\sqrt{2e^{j+1/2}}S_{h,m}^{j+1/2}. \tag{10}$$

The stability functions are specified after Galperin et al. (1988). Formulation of the TKE equation is fairly conventional and described in appendix A. It involves a careful treatment of moist thermodynamic processes, and the assumption that in case of an SCBL, all the longwave (LW) radiative flux divergence in the uppermost cloud-containing layer occurs at cloud top [Eq. (A14)]. To obtain realistic profiles of TKE in buoyancy-driven boundary layers, the transport of TKE is greatly enhanced compared to MY82 by using a TKE diffusivity of

$$K_e = \eta_{T_e}K_m, \tag{11}$$

where K_m is the geometrically averaged eddy viscosity between adjacent flux levels (Stevens et al. 1999; Patankar 1980) and $\eta_{T_e} = 5$ [Eq. (A7) and section 6].

b. Turbulent length scale

Realistic simulation of both convective and stable PBLs with a TCM requires a suitable specification of the master length scale. A variety of approaches appear in the TCM literature. In a convective PBL, the eddy scale is usually taken proportional to the PBL depth, while in a stable PBL it may be much smaller. We implemented the Blackadar length scale (Blackadar 1962):

$$l = kz/(1 + kz/\lambda), \tag{12}$$

with k the von Kármán constant, set to 0.4. To achieve the observed scaling of TKE in a deepening dry-convective PBL, we have chosen the asymptotic length scale λ proportional to the PBL depth z_i:

$$\lambda = \eta_l z_i \quad \text{with } \eta_l = 0.085 \tag{13}$$

(see results of section 6). This also gives fine simulations of well-mixed SCBLs and stable PBLs.

In the situation where the PBL is decoupled—we present the characteristics of a decoupled boundary layer in section 7b—a parcel length scale reflecting the internal stratification of the boundary layer is theoretically more appropriate. Therefore, we have also implemented a length scale similar in spirit to that proposed by Bougeault and Lacarrère (1989). We slightly modify their model by letting the local velocity scale of the parcels in unstable layers always be the local $e^{1/2}$. This prevents parcels from buoyantly accelerating to unrealistic vertical velocities as they traverse such layers. In stably stratified layers, the parcel deceleration is calculated from its buoyancy following Bougeault and Lacarrère (1989). Parcels are assumed to reach a height at which their vertical velocity goes to zero. The distances reached by the upward and downward parcels before reaching zero vertical velocity—or the PBL top/base—are, respectively, l_u and l_d. The parcel length scale is finally

$$l_p = \eta_l(l_u + l_d), \tag{14}$$

and to account for the presence of a surface layer, the turbulent length scale is set to

$$l = kz/(1 + kz/l_p). \tag{15}$$

If the PBL is a single convective layer, $l_p = \eta_l z_i$ and

(15) is equivalent to (12). However, if internal stratification of the PBL is strong enough, l_p can locally scale with the depth of each convective layer with the proportionality factor η_l. Throughout this paper, the model performance is evaluated using the Blackadar length scale [Eq. (12)]. In section 7b, we investigate the sensitivity of simulated decoupling to the use of the parcel length scale.

3. PBL entrainment

Convective boundary layers are usually topped by a stratified entrainment interface, in which large-eddy motions drive smaller entraining eddies that incorporate free-tropospheric air into the PBL. In this section we describe our parameterization for entrainment. In section 4 we will discuss how to implement this or another entrainment parameterization into the TCM.

a. Specification of entrainment parameterization

We use a Turner–Deardorff closure (Turner 1973) to calculate the entrainment rate w_e. This involves the specification of an eddy length scale L and velocity scale U:

$$w_e = AU/\mathrm{Ri} = AU^3/(L\Delta_i b), \tag{16}$$

where A is a nondimensional parameter called the entrainment efficiency, $\Delta_i b = g\Delta_i\theta_v/\theta_{v,0}$ is the buoyancy jump across the inversion, and $\mathrm{Ri} = L\Delta_i b/U^2$ is a bulk Richardson number. In our parameterization, we follow (A13), neglecting the generally small contribution of liquid water to the inversion stability and approximating $\Delta_i\theta_v \approx \Delta_i\theta_{vl}$, where $\theta_{vl} = \theta_l(1 + 0.608q_t)$ is the liquid water virtual potential temperature, an adiabatically conserved variable for reversible processes that reduces to θ_v in unsaturated air.

b. Integral closure

For a purely convective boundary layer, Deardorff (1976) proposed to take $L = z_i$ and U equal to the convective velocity scale accounting for all buoyancy production terms within the PBL:

$$U^3 = 2.5\int_{p_s}^{p_i}\overline{w'b'}\,\frac{dp}{g}. \tag{17}$$

Because U and L are scales based on the entire PBL, we call this an integral closure. Nicholls and Turton (1986) proposed, based on a fit to observations and laboratory experiments of dry CBLs and SCBLs,

$$A \equiv A_I = a_{1I}\times(1 + a_{2I}E), \qquad a_{1I} = 0.2,$$

$$a_{2I} = 60 \quad \text{with } E = \left(1 - \frac{\Delta_m b}{\Delta_i b}\right). \tag{18}$$

Here $\Delta_m b$ is the linearized average buoyancy of all possible mixtures between purely cloudy air and purely free-tropospheric air, relative to the cloudy air. The term $a_{2I}E$ determines the evaporative enhancement of entrainment. In appendix B, we relate E to cloud-top liquid water and $\Delta_i\theta_{vl}$, a necessary step for implementation of this parameterization. Whether this entrainment parameterization approach is appropriate, and whether this parameterization for A represents the evaporative cooling feedback appropriately is a matter of debate; other approaches could be used in its place (e.g., Lock and McVean 1999; Moeng et al. 1999; van Zanten et al. 1999). Here, we focus on a variant of this approach (a local entrainment closure) that can naturally be generalized to decoupled PBLs or sheared PBLs.

c. Local entrainment closure

In this approach, eddy length and velocity scales from just below the inversion (superscript 'i') are used in the Turner–Deardorff closure. For a 1.5-order TCM, we can choose $L = l^i$ and $U = \sqrt{e^i}$ in (16) to obtain the following local entrainment closure:

$$w_e = A_L\frac{e^i\sqrt{e^i}}{l^i\Delta_i b}. \tag{19}$$

At the inversion, the eddy length scale l^i is characteristic of the size of the eddies generating entrainment. Hence, with the Blackadar length scale model,

$$l^i = kz_i/(1 + kz_i/\lambda). \tag{20}$$

With the parcel length scale model we have $l_u^i = 0$, $l_p^i = \eta_l l_d^i$, and $l_i = kz_i/(1 + kz_i/l_p^i)$. The entrainment efficiency A is chosen to have the same form as (18),

$$A \equiv A_L = a_{1L}\times(1 + a_{2L}E). \tag{21}$$

LESs of dry convective boundary layer (see section 6) imply $a_{1L} = 0.16$. Due to the different TKE profiles for stratocumulus-topped PBLs compared to dry convective PBLs, the optimal match of the local entrainment parameterization with the integral closure is achieved with $a_{2L} = 15$, rather than 60, as discussed in section 7a.

4. Implementation of entrainment parameterization

In reality, entrainment and vertical advection cause the boundary layer depth to vary continuously in time. How is this best represented in a model discretized on a finite set of grid points? We compare three different implementations: a prognostic inversion, a diagnostic inversion, and a flux-level restricted inversion implementation (see Fig. 1). All of these approaches share some features. It is assumed that the convective PBL is topped by an infinitely thin inversion at some height $p_i(t)$, across which the thermodynamic variables have jumps $\Delta_i\theta_l(t)$ and $\Delta_i q_t(t)$ that must be determined at each time step. If $M + \frac{1}{2}$ indexes the highest flux level at or below the inversion, profiles in conserved variables are assumed to be well mixed from $p_{M-1/2}$ to p_i. The

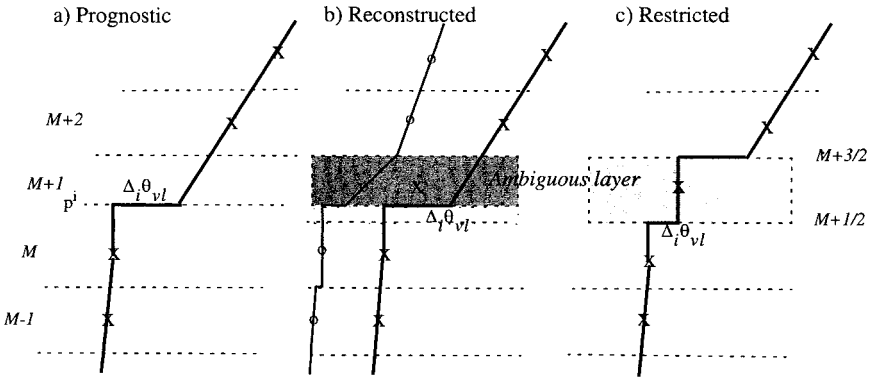

FIG. 1. Sketch of the three approaches described in the text for treating the inversion in a numerical model: (a) prognostic inversion, (b) reconstructed inversion, and (c) flux-level-restricted inversion. Dashes indicate flux levels, ×'s are the gridpoint values of θ_{vl}, and ○ denotes the profile of another arbitrary conserved scalar X. In (b) boundary layer air present in $M + 1$ is represented by a light shade and free-tropospheric air by a darker shade.

TCM is used to compute the fluxes at and below level $M - \frac{1}{2}$, and the entrainment parameterization is used to compute the fluxes at p_i. Fluxes at $M + \frac{1}{2}$ are computed in different ways depending on the implementation approach chosen (see later). The turbulent fluxes of any conservative variable X at p_i are (Lilly 1968)

$$\overline{w'X'}^i = -w_e\Delta_i X. \tag{22}$$

We now discuss each of the approaches in turn.

a. Approach 1: Prognostic inversion

In the prognostic inversion approach, the inversion pressure p_i moves continuously with time according to

$$\frac{D_h(p_i - p_s)}{Dt} = \omega_e + \overline{\omega}(p_i) \tag{23}$$

(the cumulus mass flux across the inversion would also appear on the right-hand side if present). If the inversion lies between thermodynamic levels p_M and p_{M+1}, flux level $M + \frac{1}{2}$ is set to p_i. Other flux levels are at their nominal fixed pressures. If p_i rises above the next thermodynamic level p_{M+1}, $p_{M+3/2}$ is set to p_i, and $p_{M+1/2}$ becomes a flux level internal to the PBL where the TCM is used to compute turbulent fluxes. Advantages of this approach are (i) that cloud liquid water can be diagnosed fairly precisely from the profiles in conserved variables and saturation mixing ratio below the inversion height, (ii) that inversion jumps in conservative variables are physically realistic, and (iii) that cloud properties vary quasi-continuously as the inversion moves up and down. This enables proper accounting for entrainment drying/warming of the PBL, and accurate computation of the cloud–radiation interactions. The main disadvantage of this approach is that it is impractical to implement in a three-dimensional host numerical model, in which other processes such as horizontal advection are computed on a fixed grid.

b. Approach 2: Reconstructed inversion

The concept of reconstructing the inversion properties (height and jumps) from grid points profiles was proposed to us by B. Stevens. It attempts to retain the advantages of the prognostic inversion but using a fixed grid. It is useful to first discuss how a sharp inversion that may continuously rise or sink is represented within a fixed grid (Stevens et al. 1999; appendix C). The ×'s in Fig. 1b show the mean values of a particularly significant conserved variable, θ_{vl}, over each fixed grid layer, corresponding to the θ_{vl} profile shown in Fig. 1a. The value of θ_{vl}^{M+1} in the *ambiguous layer* $M + 1$ (Stevens et al. 1999) that includes the inversion is a weighted average of below-inversion and above-inversion profiles of θ_{vl}. Other conserved scalars X will have qualitatively similar behavior (Fig. 1b). If the inversion rises through the ambiguous layer, X^{M+1} will evolve toward its below-inversion value, as more of the ambiguous layer is made of PBL air. The turbulent fluxes of X are zero by definition at flux level $M + \frac{3}{2}$ atop the ambiguous layer, and are diagnosed at flux level $M + \frac{1}{2}$ by calculating entrainment fluxes at p_i and assuming linear variation of total energy, water, and momentum fluxes between p_i and $p_{M-1/2}$. The flux convergence in $M + 1$ is how entrainment contributes to the tendency of X^{M+1}.

The reconstructed inversion algorithm attempts to reconstruct the profiles of the variables in the ambiguous layer from their gridpoint value, and to deduce w_e and the entrainment fluxes at the inversion. It is based on writing conservation equations for conserved variables in the ambiguous layer using upward and downward extrapolation (see the detailed presentation in appendix C). Once these profiles are known, saturation water vapor pressure and cloud liquid water and cloud fraction (appendix D2) can also be precisely estimated and passed to the radiation scheme.

c. Approach 3: Restricted inversion

The final, simplest approach, is to calculate the inversion jumps based on the difference between the adjacent grid points:

$$\Delta_i X = X^{M+1} - X^M. \tag{24}$$

Because the ambiguous layer $M + 1$ is a combination of PBL and free-tropospheric air, this jump may be much smaller than the true inversion jump. Since our entrainment closure correspondingly overestimates w_e [it varies as $(\Delta_i \theta_{vl})^{-1}$], entrainment fluxes at $p_{M+1/2}$ obtained from (22) remain meaningful (see section 7a). The inversion cannot explicitly rise due to entrainment, but the turbulent fluxes act to mix layers M and $M + 1$ with an ''equivalent diffusivity'' $K = w_e \delta^{M+1/2} z$. Acting unopposed, this would systematically bring the properties of the ambiguous layer toward those of the PBL, reducing the stratification at flux level $M + \frac{1}{2}$ until ultimately the diagnosed PBL top jumps up to $M + \frac{3}{2}$. Note that when both the ambiguous layer and the boundary layer top are saturated, the evaporative cooling efficiency is set to zero.

5. Vertical advection

Around the inversion, conserved variables X often have large gradients, so the advection scheme in a host GCM may produce large discretization errors. In a conventional $E - l$ model for example, Lenderink and Holtslag (2000) have shown that this leads to unrealistic entrainment rates, especially when mean subsidence is strong. For our model, vertical advection is also a concern for the reconsructed and restricted inversion implementations. In these implementations, there is an ambiguous layer that is interpreted as a combination of below-inversion and above-inversion air. This leads to a natural way to handle vertical advection across the ambiguous layer. We write

$$\overline{\omega}\frac{\partial \overline{X}}{\partial p} = \frac{\partial \overline{\omega X}}{\partial p} - \overline{X}\frac{\partial \overline{\omega}}{\partial p}, \tag{25}$$

which is discretized as

$$\left(\omega \frac{\partial X}{\partial p}\right)^j = \frac{\delta^j(\omega X)}{\delta^j p} - X^j \frac{\delta^j \omega}{\delta^j p}. \tag{26}$$

Different schemes (e.g., centered, upwinded, etc.) correspond to different choices for discretizing ωX at flux levels. However, within the ambiguous layer, we have described how to reconstruct a profile of X, including a discontinuity at the inversion. This profile dictates the values of $X^{M+1/2}$ and $X^{M+3/2}$ at the flux levels bounding the ambiguous layer. At the top of the ambiguous layer $M + 1$, the air comes from above the PBL and $X^{M+3/2}$ is computed through downward extrapolation (see appendix C). At $M + \frac{1}{2}$, as the air comes from inside the PBL, we set $X^{M+1/2} = X^M$, unless the inversion lies exactly at $p_{M+1/2}$, in which case we set $X^{M+1/2} = X^{M+1}$. This discretization of ωX at $p_{M+1/2}$ and $p_{M+3/2}$ is used both with the reconstructed and restricted inversion approaches. Thus, subsidence strongly affects the ambiguous layer (corresponding to a lowering inversion) but does not create spurious gradients inside the PBL. At flux levels not adjoining the ambiguous layer, the host model advection scheme is used to calculate the advective fluxes. For our simulations, we use the scheme presented in appendix D, section a. In section 7c(2), we compare the performance of this scheme with an upwind advection scheme used at all flux levels, including those adjoining the ambiguous layer.

6. Simulations of a dry CBL

The dry convective boundary layer (CBL) heated from below has been extensively studied both observationally, using water tanks, and with LES, with consistent results. In this section, we show how simulations of a dry CBL with our parameterization determine the convective length scale parameter η_l [see Eq.(15)], the turbulent transport parameter η_{T_e} [see Eq. (A6)] and the dry entrainment efficiency parameter a_{1L} for the local entrainment closure. In addition, we use it as an initial test of the skill of the three implementations of entrainment at varying grid resolutions. We have also performed successful simulations of a diurnal cycle. We will not discuss these simulations, since in a stable boundary layer the entrainment closure is not used and the model reduces to a standard 1.5 TCM, whose performances and sensitivity to model formulation can be found in the literature (see e.g., Brasseur et al. 1998).

We initialize the model with no moisture ($q_t = 0$) or TKE, and a vertical profile of θ_l ($=\theta$) consisting of a 500-m-deep mixed layer capped by a 4-K inversion, with uniform static stability of 3.4 K km^{-1} above. A steady surface heat flux of 100 W m^{-2} is imposed throughout the 6-h simulation.

a. Specification of η_l and η_{T_e}

Since the TKE dissipation rate is related to the turbulent length scale, this can be used to determine η_l. The vertical distribution of TKE is primarily controlled by the efficiency of TKE transport, that is, η_{T_e}. We used results published by Moeng and Sullivan (1994) to determine the best-fit values of η_l and η_{T_e}, for our model. Figure 2 shows a time–height section of θ_l simulated by our model with $\eta_l = 0.085$, $\eta_{T_e} = 5$, the integral closure (17), the prognostic inversion model, and 15-mb grid spacing. The thick black line indicates the inversion. During the first hour, the TKE grows into balance with the surface heating. Thereafter, the inversion smoothly rises through the grid. Figure 3 shows the vertical profile of scaled TKE (e/w_*^2), and the vertical profiles of scaled buoyancy production and transport at three times, showing that these profiles grow in a self-similar fashion. By construction, the entrainment clo-

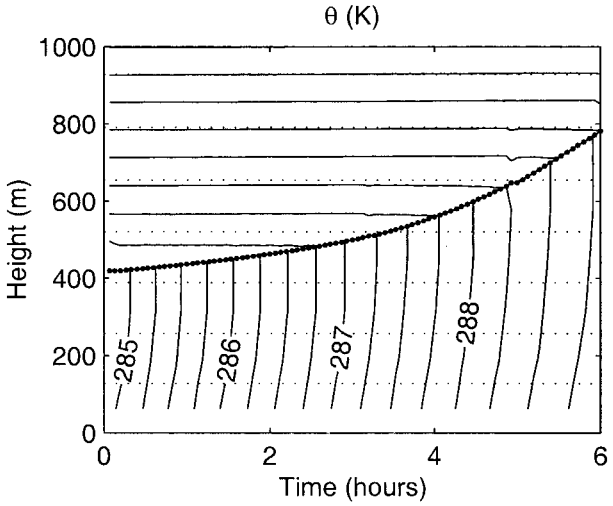

FIG. 2. Time–height section of θ in the dry CBL simulation using the integral entrainment closure and prognostic inversion. Horizontal thin-dotted lines show the flux levels, and the heavy-dotted line is the reconstructed inversion pressure.

sure (14)–(16) ensures that the downward buoyancy flux at the inversion is 0.2 of the upward surface buoyancy flux, in accord with observations and LES. The model maintains a self-similar structure in TKE throughout the deepening of the CBL. (If a constant asymptotic lengthscale λ were used in the Blackadar formulation, this would not be the case.)

As shown by Moeng and Wyngaard (1989), and earlier discussed by Zeman and Lumley (1976), buoyancy effects and gradients in vertical velocity variance, rather than down-gradient diffusion of e, are the main contributors to the budget of $\overline{w'e'}$. However, LES does show that in dry, radiatively driven, and stratocumulus topped boundary layers TKE maximizes where buoyancy production is largest; but the vertical variations of TKE are smaller than the variations in buoyancy production. Thus, although the detailed structure of TKE is not well represented by downgradient diffusion, its broad features are consistent with a diffusion model. By taking $K_e = \eta_{T_e} K_m$ with $\eta_{T_e} = 5$, we are able to reproduce the TKE profile fairly well in both CBLs and SCBLs. For instance, with this K_e, the vertical profile of TKE transport simulated by the model compares well with Moeng and Sullivan's (1994) formulation (also shown in Fig. 3b).

b. Local entrainment closure

In a dry CBL, the master length scale is $\eta_l z_i$. Hence the dry entrainment efficiency for local entrainment closure, a_{1L}, can be estimated from (19) and (16):

$$a_{1L} = a_{1I}\eta_l (e^i/w_*^2)^{-3/2}. \tag{27}$$

With $a_{1I} = 0.2$, $\eta_1 = 0.085$, and $e/w_*^2 \sim 0.22$ [as shown by Moeng and Sullivan's (1994) LES], we obtain $a_{1L} = 0.16$. A simulation using the local entrainment closure with this value for a_{1L}, inversion reconstruction, and 15-hPa vertical resolution is almost indistinguishable from the simulation with the integral closure discussed above.

c. Sensitivity to entrainment implementation and vertical resolution

Figure 4 shows the inversion height for the three implementations of the entrainment closure, and 15-mb vertical resolution typical of many regional models. Figure 5 shows corresponding results with a coarser 31-level vertical grid, representative of current GCMs. All three approaches deepen the CBL at a similar rate following surface warming at both fine and coarse resolution. The scaled model profiles of TKE and buoyancy production look almost identical to those in Fig. 3, even with 31-level vertical resolution and a flux-level-restricted inversion. In contrast, a recent model intercomparison by Ayotte et al. (1996) found that most currently used GCM parameterizations were not properly simulating the buoyancy flux profile in the CBL.

7. Marine stratocumulus advecting over rising SST

The main basis for evaluating different versions of the moist PBL parameterization presented in this paper

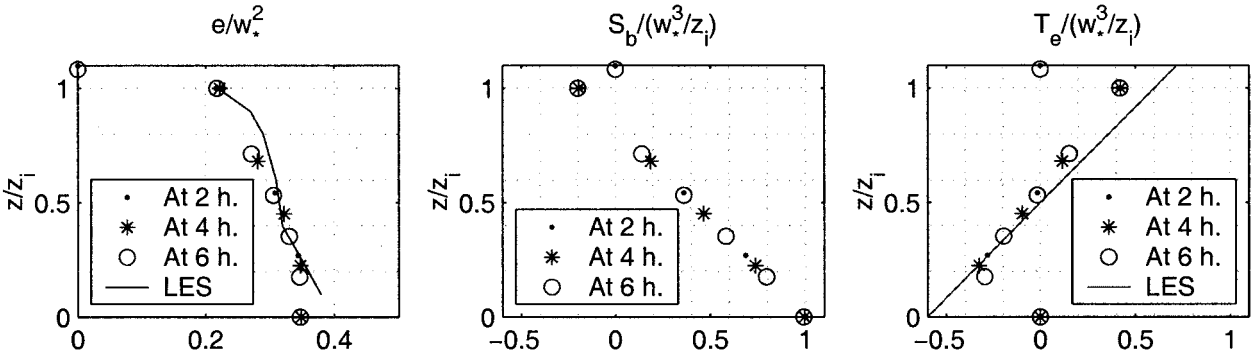

FIG. 3. Scaled profiles of (a) normalized TKE, (b) buoyancy flux, and (c) transport from the model at three different times (symbols), and from Moeng and Sullivan's (1994) LES (lines).

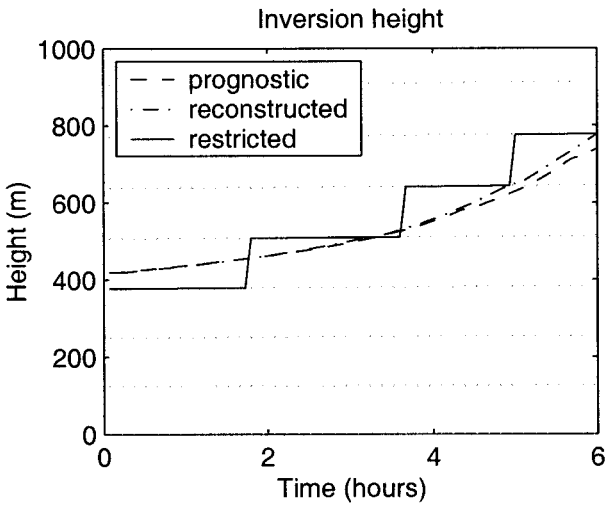

FIG. 4. Inversion height for CBL simulations with 15-mb grid spacing, comparing the three proposed inversion implementations.

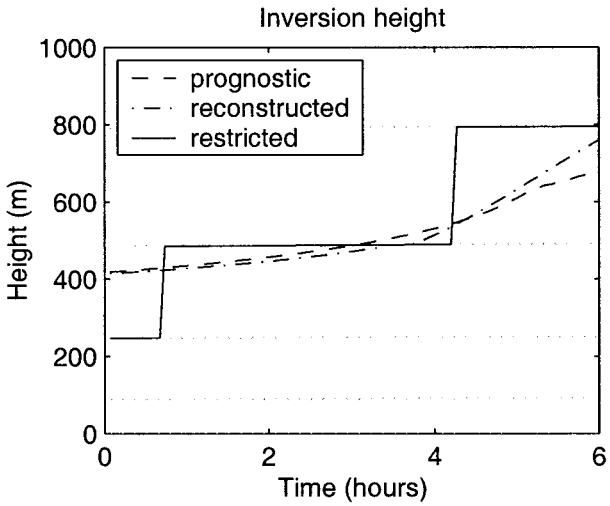

FIG. 5. As in Fig. 4 but with the 31-level model.

is an idealized simulation of an SCBL advecting over rising SST. We test the model's ability to sustain stratocumulus cloud of realistic thickness at GCM vertical resolution, and to simulate the decoupling of the cloud layer from the subcloud layer that is observed to follow both daytime cloud solar absorption (Nicholls 1984; Nicholls and Leighton 1986; Hignett 1991) and systematic SST increase (Bretherton et al. 1995; Krueger et al. 1995; Bretherton and Wyant 1997). This is a necessary precursor to formation of shallow cumulus within the SCBL, which are thought to lead to the ultimate breakup of the capping stratocumulus layer (Wyant et al. 1997).

Following Bretherton and Wyant (1997), each simulation is initialized with a shallow, well-mixed SCBL over a relatively cool (286 K) SST, topped by a strong (13 K) inversion. The SST is increased at 1.5 K day^{-1}, while the free-tropospheric thermodynamic sounding is held fixed. This mimics the changing boundary conditions encountered by a subtropical SCBL advected equatorward by the trade winds off the west coast of a continent. Large-scale subsidence is specified assuming a constant divergence of 3×10^{-6} s^{-1}. Simulations start at midnight local time and last for 5 days. Table 1 gives other relevant boundary conditions, while Table 2 summarizes the model configurations used in the different simulations. The model time step is 8 min.

a. Simulations using 15-mb vertical resolution

1) INTEGRAL VERSUS LOCAL ENTRAINMENT CLOSURE

Figure 6a shows the time evolution of cloud base, cloud top, and surface lifting condensation level (LCL) during simulation IP. During days 1–3, the simulation exhibits a realistic diurnal cycle of cloud thickness, 300 m in early morning, thinning to 150–200 m by noon, comparable to observations reported during the First International Satellite Cloud Climatology Program Regional Experiment (FIRE) (Hignett 1991). In this figure, the internal stratification of the SCBL can be assessed from the difference between the surface LCL and cloud base. During the first three nights, these are nearly coincident, implying the SCBL is well mixed. During the first three mornings, surface LCL drops slightly while cloud base rises, indicating a slightly less well-mixed SCBL. Later in the simulation, the now deeper SCBL remains stratified or decoupled throughout the diurnal cycle, and is composed of a surface-driven convective layer, a conditionally unstable layer with intermittent turbulence, and a radiatively driven upper convective layer, as found in both observations and eddy-resolving models (Albrecht et al. 1995; Bretherton and Pincus 1995; Krueger et al. 1995). In section 7b, we will examine the feedbacks responsible for SCBL stratification in our parameterization.

Figure 6b shows results obtained with the local entrainment closure (simulation LP). For this simulation, we chose a value $a_{2L} = 15$ such that when the boundary layer remains well mixed (the first 3–4 days), LP matches the integral closure results of IP. Here, a_{2L} is smaller

TABLE 1. Large-scale and boundary conditions used in the deepening/warming experiment.

Parameter	Value
Surface pressure (mb)	1015
SST (K)	286.2 + (1.5 K day^{-1})
Initial θ_l in the PBL (K)	284.8
Initial q_t in the PBL (g kg^{-1})	7.69
Initial θ_l above the PBL (K)	295 + 3.36 z (z in km)
Initial q_t above the PBL (g kg^{-1})	3
Large-scale divergence (s^{-1})	3×10^{-6}
Initial p_l (mb)	949
Geostrophic wind speed (U_g, V_g)	(9, 0) m s^{-1}
Latitude	28°N
Day of year	1 June

TABLE 2. Summary of the various deepening/warming experiments. The liquid water path is the mean over a 5-day simulation.

Case	IP	LP	LD	LR	LP_{31}	LD_{31}	LR_{31}
Entrainment closure	Integral	Local	Local	Local	Local	Local	Local
Inversion implementation	Prognostic	Prognostic	Reconstructal	Restricted	Prognostic	Reconstructed	Restricted
Grid spacing	15 mb	15 mb	15 mb	15 mb	L31	L31	L31
Liquid water path (g m^{-2})	112	97	110	129	104	144	70

than a_{2I} because the concentration of buoyancy production at cloud top makes for a larger e/w_*^2 at the inversion than it does in a dry CBL. In a decoupled boundary layer, local entrainment closure is more appropriate than our integral closure, which may amalgamate buoyancy production in two dynamically isolated convective layers (see Stevens 2000). Hence, we will use the local entrainment closure in the remainder of the paper.

2) COMPARISON OF INVERSION IMPLEMENTATIONS AT 15-MB RESOLUTION

Figure 7 compares the PBL evolution with the three different inversion implementations at 15-mb vertical resolution. As in the dry convection case, simulations with prognostic and reconstructed inversions give very similar PBL evolution, though the latter exaggerates the diurnal fluctuations of inversion height. For the reconstructed and restricted inversion, we use the special treatment of vertical advection discussed in section 5. Use of upwind advection prevents the reconstructed inversion from deepening comparably to the prognostic inversion. The restricted inversion simulation also gives very satisfactory results at this resolution with our vertical advection scheme.

3) ADVECTION–RADIATION–ENTRAINMENT INTERPLAY WITH THE RESTRICTED INVERSION

When the inversion is restricted to be on a flux level, vertical advection warms/dries the ambiguous layer, while entrainment fluxes cool/moisten this layer. If entrainment is stronger than subsidence, the ambiguous layer will cool and moisten over a time step. We call this process virtual deepening. Virtual deepening results in a gradual decrease in the jumps across the inversion until the inversion Richardson number falls below its critical value, and the inversion moves up to the next flux level. Despite the gradual decrease in θ_l and q_t jumps across the inversion, Fig. 8 shows that entrainment fluxes in simulation LR do have a similar evolution as in the reconstructed inversion simulation. This reflects an important property of our entrainment closure that allows it to work successfully with a restricted inversion. With the local entrainment closure (19), the entrainment flux of any conserved scalar X can be written

$$-w_e\Delta_i X = -a_{1L}(1 + a_{2L}E)\frac{(e^i)^{3/2}}{l^i}\frac{\Delta_i X}{(g/\theta_{v,0})\Delta_i\theta_{vl}}. \quad (28)$$

As the ambiguous layer is cooled and moistened by entrainment, its X is brought toward its value at the top of the SCBL, but so is its θ_{vl} (which is another scalar conserved for adiabatic processes). Hence the ratio $\Delta_i X/\Delta_i\theta_{vl}$ remains nearly constant. The TCM maintains a fairly steady TKE during virtual deepening. If the evaporative enhancement factor E is evaluated using jumps between the PBL top and the level above the ambiguous layer, it is also insensitive to virtual deepening. Hence, the entrainment fluxes are insensitive to the virtual deepening process, except for a few hours preceeding the jump of the inversion to the next flux level. During this

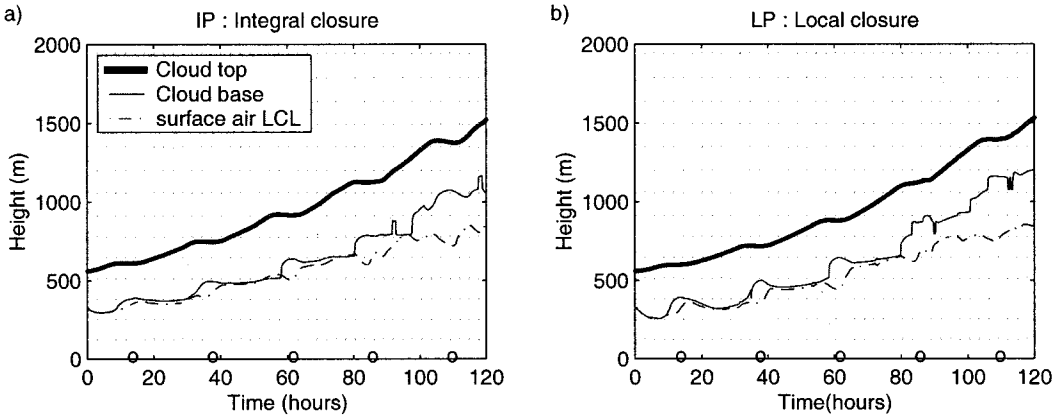

FIG. 6. Evolution of PBL top (thick solid line), cloud base (thin solid line), and LCL of near-surface air (dash–dot line) in (a) simulation IP and (b) simulation LP. Circles on the abscissa indicate 1200 local time.

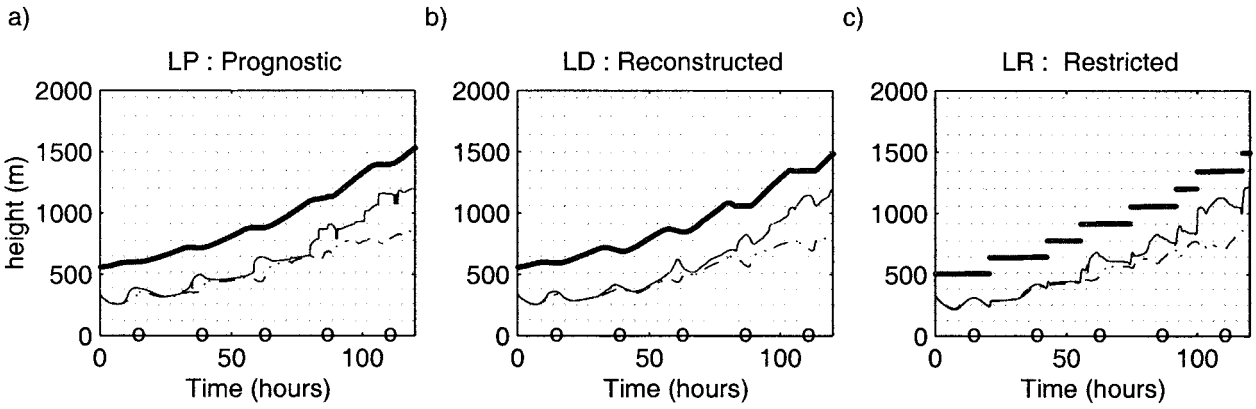

FIG. 7. As in Fig. 6 but for three inversion implementations of the local entrainment closure.

period of time, the ambiguous layer is significantly saturated. Radiation then adds up with entrainment to cool the ambiguous layer, and therefore, does not contribute to TKE generation inside the boundary layer. As the evaporative cooling efficiency is also set to zero if the ambiguous layer is saturated, entrainment fluxes significantly decrease shortly before the inversion jumps to the next flux level.

b. Mechanisms of SCBL response to external forcings

In this section, we discuss the response of the simulated SCBL to the diurnal cycle of insolation and to SST rise, and present how decoupling occurs in the TCM. The primary forcings are radiative flux divergence and surface fluxes, shown in Fig. 9a for simulation LD (other simulations are similar). The strong diurnal cycle in the net radiative flux divergence over the SCBL is due to cloud shortwave absorption. Surface sensible heat fluxes are small, while latent heat fluxes rise threefold over the simulation. Figures 9b and 9c show some measures of the SCBL response to these forcings. The convective velocity scale w_* (computed from the vertically integrated buoyancy flux) responds to the strong diurnal cycle in net cloud radiative cooling, but does not have a large trend over the simulation. The entrainment rate w_e has a corresponding diurnal cycle and rises steadily as the inversion weakens from 13 to 7 K with the warming of the boundary layer. These variations in w_e contribute to keep entrainment fluxes of θ_l in close balance with the net SCBL radiative flux divergence (Bretherton and Wyant 1997). The minimum in buoyancy flux across the boundary layer ($\overline{w'b'}|_{c^-}$) also shows strong diurnal modulation during the first three days of simulation. It becomes significantly negative during daytime after three days of simulation. In the latter part of the simulation, its sensitivity to the diurnal cycle is small. The corresponding subcloud eddy diffusivity (Fig. 9c) enables stratification to build-up during daytime and during the decoupled phase of the simulation.

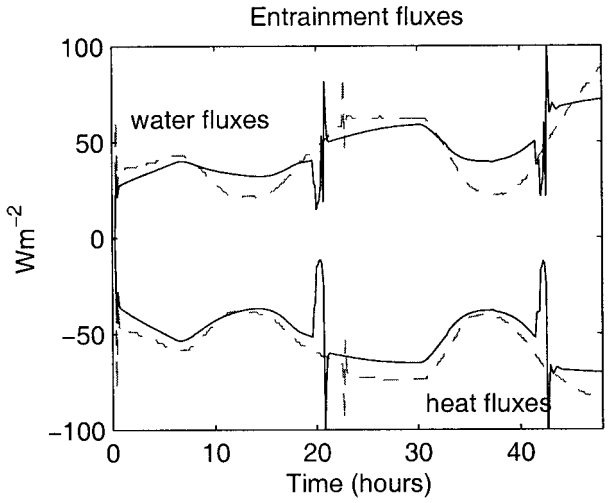

FIG. 8. Time evolution of entrainment fluxes of heat and water with a reconstructed inversion (dashed lines, simulation LD) and a restricted inversion (unbroken lines, simulation LR). Spikes at hours 22 and 45 are due to the PBL top jumping up to the next flux level.

1) DIURNAL CYCLE IN THE EARLY PHASE

During the early phase of the simulation, nighttime TKE profiles simulated by the model (Fig. 10a) are comparable to those in a typical shallow nocturnal marine SCBL observed during FIRE (Hignett 1991; Duynkerke and Hignett 1993). The simulated daytime TKE profile is somewhat larger and more vertically uniform than observed (Fig. 10a). Although environmental conditions were quite similar between FIRE and our simulation, the observed daytime cloud thinning was more pronounced than in our model. This was partly due to a strong diurnal cycle in the mean inversion height (Duynkerke and Hignett 1993), suggesting a diurnal cycle in the mean subsidence. We believe this may account for the model simulation differences, because TKE is driven mainly by buoyancy fluxes within the cloud layer, so a thinner cloud cannot support as much TKE. The proximity of the observation site with the coast may

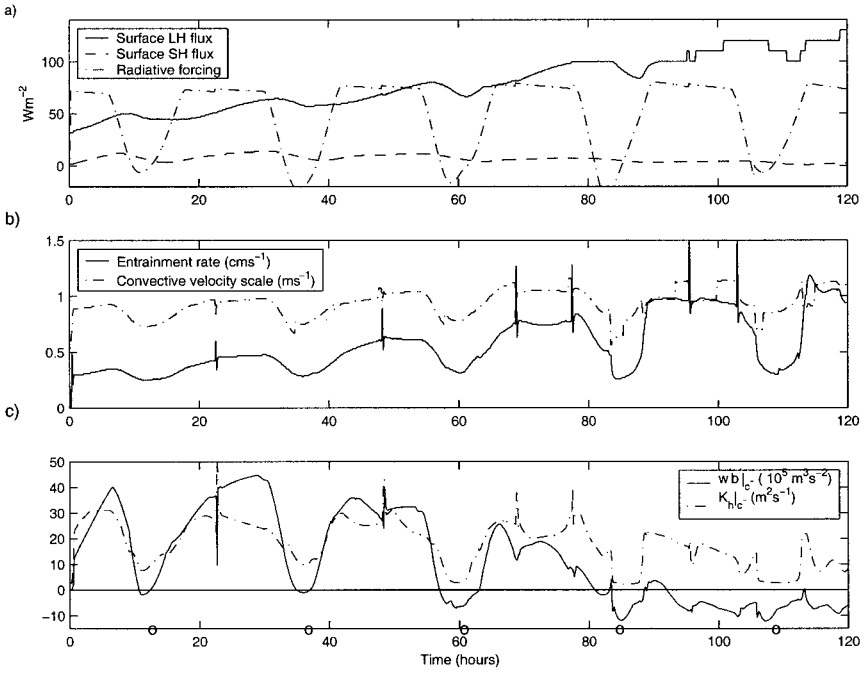

FIG. 9. Time evolution of selected variables in simulation LD: (a) surface turbulent heat fluxes and radiative forcing of the PBL (W m^{-2}), (b) entrainment rate and convective velocity scale, and (c) minimum in buoyancy flux ($\overline{w'b'}|_{c^-}$) and eddy-diffusivity ($K_h|_{c^-}$) inside the PBL.

also have an impact on the observations reported by Hignett (1991) (B. Stevens 2000, personal communication).

2) PROCESSES CONTROLLING DECOUPLING IN THE TCM

Observations (Hignett 1991; Rogers et al. 1995; de Roode and Dyunkerke 1997) and LES (Krueger et al. 1995; Bretherton and Wyant 1997; Stevens 2000) indicate that a distinct minimum in TKE and a negative buoyancy flux at the top of the surface-driven mixed layer are characteristic of the decoupled SCBL. Although the TCM realistically stratifies the SCBL during daytime and the decoupled phase, TKE does not develop a pronounced subcloud minimum (Fig. 10b). Instead, it is maintained there against buoyancy destruction and dissipation by turbulent transport (Fig. 11a). So, how is eddy diffusivity K_h suppressed at this level to produce stratification? Recall that K_h is a product of $e^{1/2}$, l, and the stability functions S_h [which are functions of normalized stratification N^2l^2/e; see Galperin et al. (1988)]. Although $e^{1/2}$ and l remain sizeable in the subcloud layer even with SCBL stratification, the S_h is rather sensitive to stratification. In neutral stratification, S_h is less than 10% as large as in strongly unstable stratification, and in weakly stable stratification seen in the decoupled phase, S_h drops a further factor of 10. Variations in S_h clearly dominate the variations in K_h in the decoupled regime (Figs. 11b–d).

3) SENSITIVITY OF DECOUPLING TO THE MASTER TURBULENT LENGTH SCALE

In the decoupled regime, a single Blackadar length scaling with the SCBL depth is no longer appropriate. Hence, we also performed a deepening/warming simulation with the Bougeault parcel-displacement-based master length scale [see Eq. (2.2)], which is sensitive to internal stratification inside the SCBL. Figure 12 shows that in the two convective layers the parcel length scales with the convective layer depth, while it drops in the stably stratified layer below the cloud base. It is smaller than the Blackadar length scale throughout the decoupled PBL. The profile of K_h has a shape similar to the one simulated with the Blackadar length scale, except in the upper convective layer where it is significantly smaller. Consequently, the upper part of the PBL is more stratified with the parcel length scale. As turbulent dissipation is proportional to l^{-1}, but buoyancy fluxes are little affected by the length scale, TKE is reduced throughout the boundary layer. This brings TKE profiles simulated by the model in the decoupled phase (Fig. 13) in better overall agreement with the profiles presented by Rogers et al. (1995) and de Roode and Duynkerke (1997). In particular the observed TKE minimum below cloud base is now well captured by the model. During these observations, characteristic of decoupled boundary layers during nighttime and daytime, a substantial fraction of the TKE was localized within cumuli rising into a stratocumulus [broken in flight 5

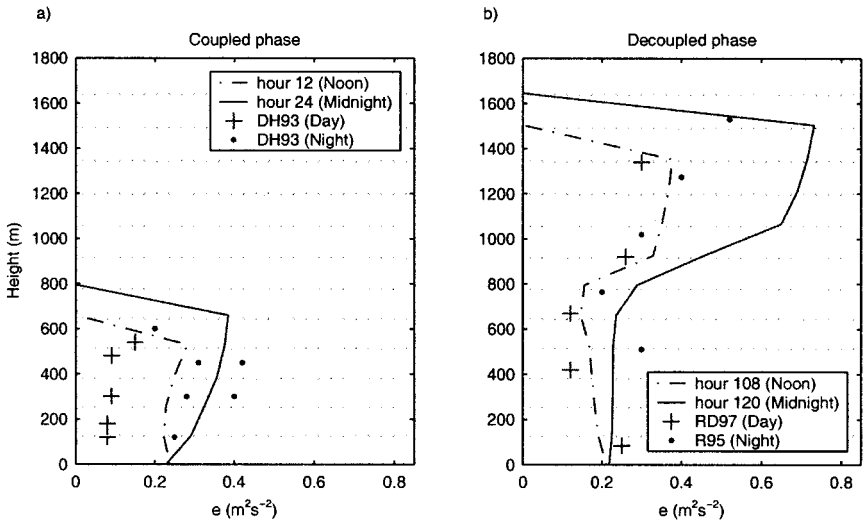

FIG. 10. Lines show hourly averaged vertical distribution of TKE ($m^2\ s^{-2}$) (a) in the coupled phase and (b) in the decoupled phase. Dots indicate nighttime-observed TKE profiles of Duynkerke and Hignett (1993) in (a) and run 2 of Rogers et al. (1995) in (b). Plus signs indicate daytime-observed TKE profiles of Duynkerke and Hignett (1993) in (a) and de Roode and Duynkerke (1997), for Atlantic Stratocumulus Transition Experiment Lagrangian flight 5 in (b). In the right panel, the height scale for the observed profiles has been scaled by $z_{i_{\text{model}}}/z_{i_{\text{observations}}}$.

of de Roode and Duynkerke (1997)]. The simulations presented here do not include an explicit parameterization of shallow cumuli. The TKE scheme imperfectly represents their effects by intermittent pulses of cloud and TKE rising from the surface LCL, but it would be more realistic to include a separate shallow cumulus parameterization. We will present results from such an approach in a forthcoming paper.

Figure 14 compares the evolution of the PBL over seven days of the deepening/warming simulation using the two length scale models. Bulk features of the PBL are remarkably insensitive to the length scale model, even though TKE and K_h explicitly depend on the length scale. One reason is that the entrainment closure (19) relates the entrainment rate to $e^{3/2}/l$, that is, turbulent kinetic energy dissipation. Averaged over the upper convective layer, dissipation balances buoyancy production, which is mainly radiatively driven and not sensitive to the turbulence scheme. Hence, the entrainment rate is insensitive to the turbulent length scale. Similarly, the stable layer can be thought of as a valve that regulates the cloud thickness so that entrainment warming (which increases for a thicker cloud as the evaporative enhancement factor E rises) stays in balance with radiative cooling. As long as some mechanism (in our parameterization the stability functions) permits this valve to form, the thermodynamic profiles are insensitive to the details of the parameterization. However, the parcel length scale enables more realistic simulation of TKE in decoupled boundary layers.

c. Low-resolution deepening/warming simulations

Low-resolution (31 level) results (Fig. 15) with the prognostic inversion approach are very similar to those presented in Fig. 7 for the high-resolution case. With the two other approaches, decreasing the resolution introduces a bias on the liquid water path (LWP) (Table 2). With the reconstructed inversion, the cloud thickness and cloud depth are too large at lower resolution, and the PBL depth is underestimated by 100 m or so. Differences in LWP are close to 30% on average over the whole simulation. This increase in cloud depth may be due to the mixed layer assumption made to reconstruct thermodynamic profiles between $p_{M-1/2}$ and p_i. At coarse resolution, it is common that the cloud base (where negative buoyancy fluxes and decoupling typically initiate) is above $p_{M-1/2}$. This may impede the development of a stable layer below cloud base, delay decoupling, enhance vertical mixing, and increase cloud depth.

With a restricted inversion, the model is still able to sustain the stratocumulus at the 31-level resolution and the PBL evolution is qualitatively similar, but the cloud is systematically too thin. The location of the Sc base is well captured, but the PBL top is underestimated, so liquid water path is only half as large on average as in simulation IP (Table 2). This leads to reduced longwave cooling across the SCBL in the coupled regime, delayed deepening, and abrupt decoupling when the cloud top jumps to the next flux level.

1) SENSITIVITY TO THE a_{2L} PARAMETER

We tried to compensate for the LWP bias of the restricted inversion approach by retuning the evaporative enhancement feedback parameter a_{2L}. Smaller a_{2L} means that for a given TKE, higher cloud-top liquid water content (a thicker cloud) is needed to generate a

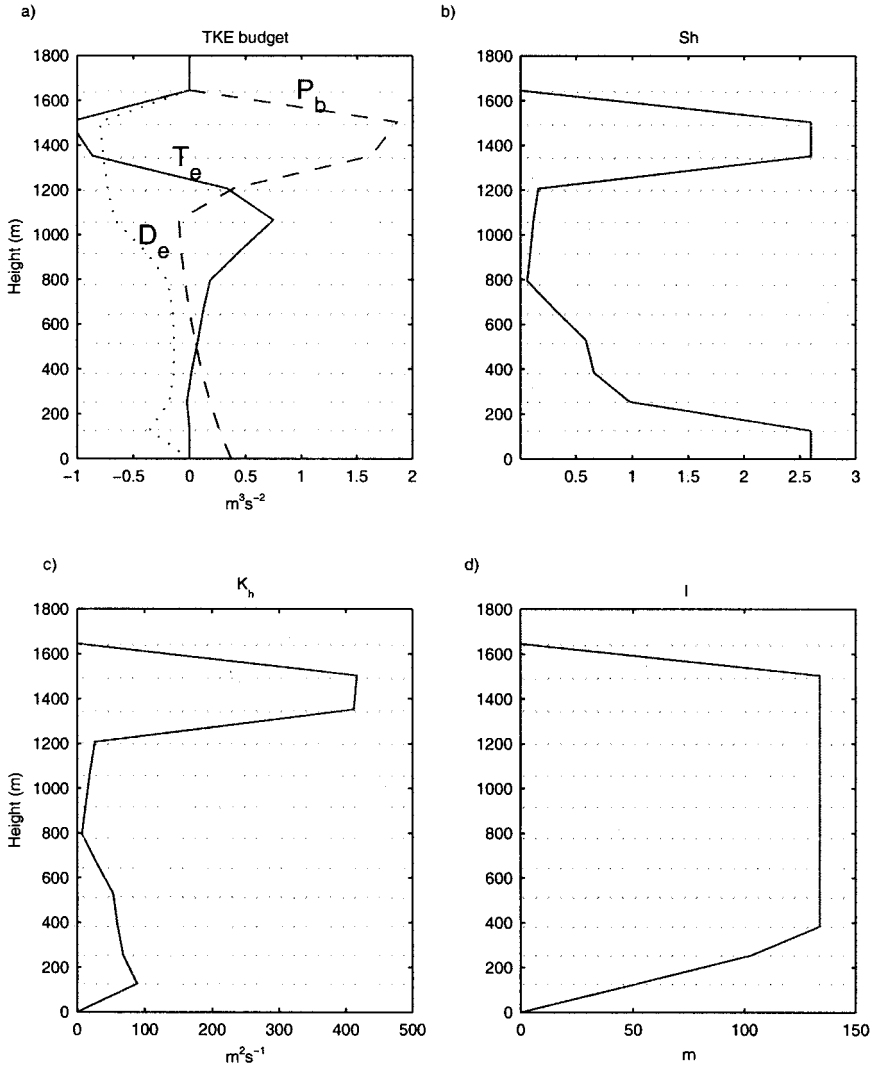

FIG. 11. Hour 120 averaged vertical distribution of (a) buoyancy production P_b, turbulent transport T_e and turbulent dissipation D_e ($m^2\ s^{-3}$), (b) S_h, (c) K_h ($m^2\ s^{-1}$), and (d) turbulent length scale (m), characteristic of the decoupled period.

given entrainment rate. Thus one might expect a_{2L} to regulate equilibrium stratocumulus cloud thickness. We show in Table 3 results obtained with $a_{2L} = 10$ and $a_{2L} = 5$. As expected, this parameter has a strong impact on the liquid water content of the cloud, which increases by a factor 1.5 with $a_{2L} = 5$. However, both the PBL top and cloud base are seriously underestimated with $a_{2L} = 5$ because the entrainment rate is too small. Consequently, the surface layer is too cold and too moist (Table 3). As the PBL remains too shallow, it also remains well mixed even over warmer SST, and cannot support a transition toward cumulus convection. Hence, retuning of a_{2L} is not advisable.

2) SENSITIVITY TO VERTICAL ADVECTION

In the ambiguous layer, vertical advection is of comparable importance to entrainment. Inversion reconstruction suggested a natural treatment of vertical advection at the flux levels bounding the ambiguous layer (section 5). However, it is obviously simpler to just use the host model vertical advection scheme throughout. To test how this would affect our results, we performed simulations similar to LD_{31} and LR_{31} but with upwind advection. For the reconstructed inversion, this fails completely. With a restricted inversion, use of upwind advection lowers the simulated liquid water path (Table 3) by an average of 40% since the PBL warms, dries, and deepens faster than with our advection scheme. This bias is of the same sense and magnitude as the bias introduced by use of a restricted inversion versus reconstructed inversion. Other advection schemes tend to perform worse; hence use of our advection scheme around the ambiguous layer is important in obtaining reasonable results, especially with coarse vertical res-

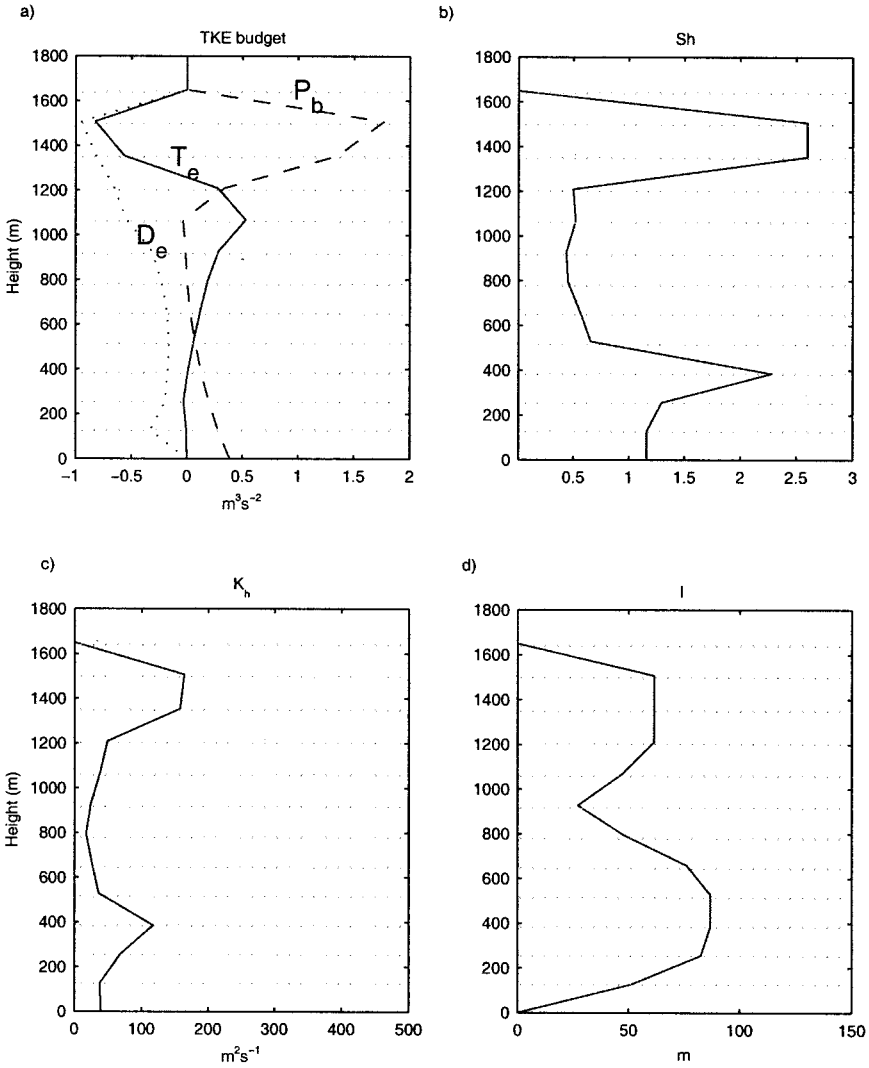

FIG. 12. As in Fig. 11 but with the parcel length scale.

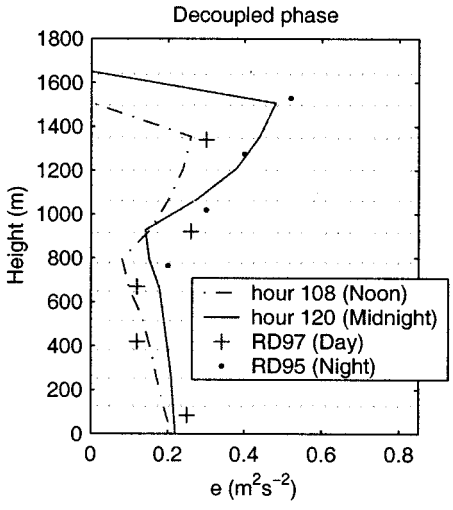

FIG. 13. As in Fig. 10b but with the parcel length scale.

olution. When the subsidence is larger than the simulated entrainment rate, the model does not tend to lock the PBL top on a flux level, as is the case with the $E - l$ model (Lenderink and Holtslag 2000), either with our advection scheme or upwind advection. This again illustrates the utility of treating the inversion using an explicit entrainment parameterization.

8. Conclusions

We present a new PBL parameterization for large-scale models that combines 1.5-order turbulent closure within the PBL with an explicit entrainment parameterization at the top of a convective PBL. The parameterization is designed to provide efficient and accurate simulations of cloud-topped boundary layers given limited vertical resolution. The convective PBL is assumed to be topped by an infinitely thin inversion where we apply an entrainment closure. We use a Turner–Dear-

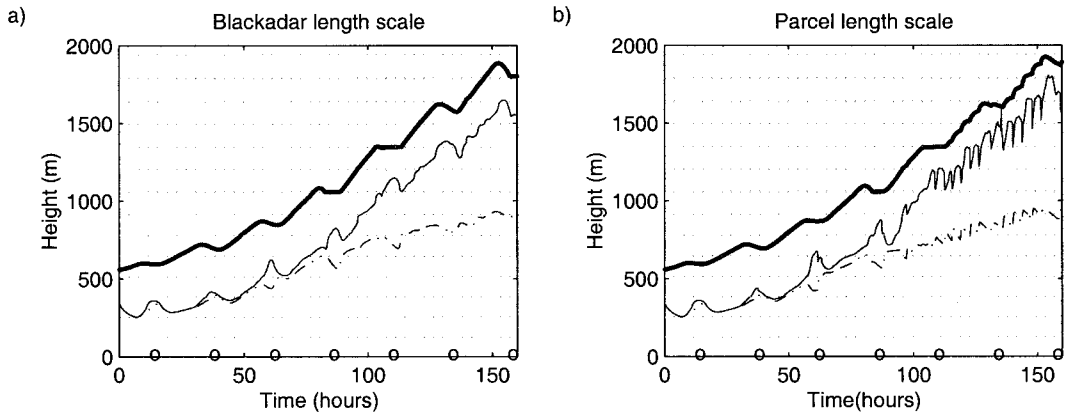

FIG. 14. As in Fig. 6 but with two different length scale models: (a) the Blackadar model, and (b) the parcel length scale. Simulations are carried over 7 days to emphasize model behavior in the decoupled phase.

dorff entrainment parameterization that relates entrainment rate to boundary layer TKE, an eddy length scale, and inversion strength. Following Nicholls and Turton (1986), the entrainment rate into cloud-topped boundary layers is considerably enhanced by mixing-induced evaporative cooling. The formulation of the TCM is classical [it is based on the Mellor and Yamada (1982) formulation and uses moist conserved thermodynamic variables] except for the following important feature: in the case of an SCBL, the cloud-top LW radiative flux divergence is all applied at the inversion, rather than being distributed through a grid layer. This helps ensure a reasonable profile of buoyancy production even at coarse vertical resolution. The vertical transport of TKE has also been artificially increased in order to obtain proper matching of the TKE profile with LES of various convective PBLs.

We compared three different implementations of the entrainment closure in a single-column model. The prognostic inversion implementation provides good simulations of cloud-topped and dry convective boundary layers at all resolutions tested. Like some GCMs, it uses an inversion-following coordinate level. Despite its good performance in our simulations, the prognostic inversion has potential difficulties for GCM use. First, it is not compatible with the fixed vertical grid levels used in most GCMs. Second, in some situations the PBL top may discontinuously change in time or space, requiring very careful treatment of a prognostic inversion. Examples include decay of the daytime dry convective boundary layer over land or PBL decoupling into two distinct turbulent layers.

The two other approaches, because they are diagnostic in nature, make the PBL scheme more widely applicable to a whole range of situations. The grid levels are fixed and at the PBL top there is an ambiguous layer whose layer-mean properties are intermediate between the PBL top and the free troposphere. We can interpret the ambiguous layer as a partial layer of PBL air overlaid by free-tropospheric air. This structure is explicitly diagnosed by the reconstructed inversion implementation. This provides simulations nearly as good as the prognostic inversion. Its implementation in a large-scale model requires that vertical advection and the cloud scheme account for the presence of PBL air in the ambiguous layer. The restricted inversion approach, in

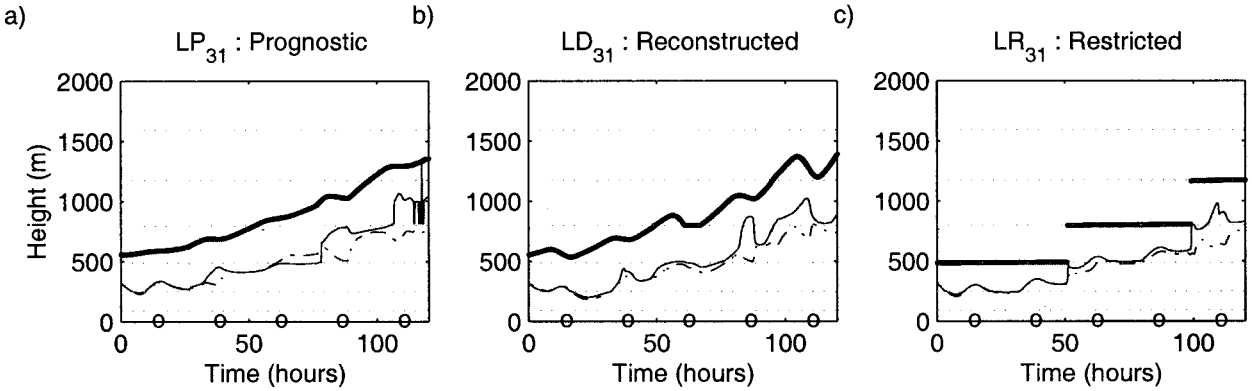

FIG. 15. As in Fig. 7 but with the 31-level model.

TABLE 3. Summary of the sensitivity experiments performed at low resolution with the restricted inversion. The boundary layer top (z_i) and the LWP are 5-day averaged. Here, $\Delta_s\theta_l$ is the surface value minus the value of θ_l at the first grid level and is computed at the end of the 5-day simulation.

Parameter	LD	LD_{31}	LR_{31}	LR_{31} $a_{2L} = 10$	LR_{31} $a_{2L} = 5$	LR_{31} Upwind advection scheme
z_i3 (m)	915	875	713	669	619	730
LWP (g m^{-2})	110	144	70	86	115	47
$\Delta_s\theta_t$ (K)	0.25	0.58	0.52	0.94	1.36	0.42

which the internal structure of the ambiguous layer is ignored, is simplest to implement in a large-scale model. It produced good simulations of penetrative dry-convective boundary layers at both vertical resolutions tested (15 mb and a coarser 31-level variable mesh). For stratocumulus, it also produces very good results at l5-mb resolution. However, as it systematically truncates the PBL top below its actual value, the restricted inversion produces stratocumulus clouds with too low a liquid water path at lower vertical resolution. This bias might be correctable by applying the ''profile reconstruction'' algorithm solely for estimates of liquid water path, which would then be passed to the radiation scheme.

With a restricted or reconstructed inversion, the model performance is strongly dependent on the vertical advection scheme. We propose a correction to the advective fluxes at the flux levels bounding the ambiguous layer inspired by profile reconstruction. Our approach for vertical advection is essential for obtaining good results with the reconstructed inversion; for the restricted inversion, it largely improves the results compared to an upwind scheme (giving 50% higher liquid water path).

In theory, our PBL scheme is compatible with a variety of entrainment parameterizations, and in fact there is considerable debate about the most appropriate parameterization for entrainment into an SCBL. However, the success of the scheme with a restricted inversion does depend on three important features of our entrainment parameterization. First, the entrainment rate is inversely proportional to the jump in a conserved variable (θ_{vl}), so the entrainment fluxes are not sensitive to the fraction of boundary layer air in the ambiguous layer above the PBL, and do not vary spuriously as the ambiguous layer evolves. Second, the entrainment rate increases rapidly with cloud-top liquid water content due to the evaporative cooling feedback. In practice, the strength of this feedback helps regulates the cloud thickness even when the cloud is barely vertically resolved. Finally, our entrainment closure makes the PBL model quite insensitive to the particular choice of the convective length scale in the turbulent closure model.

Acknowledgments. It is our great pleasure to thank Bjorn Stevens for many fruitful discussions on various aspects of this work. We are also grateful to him, David Randall, and Stephan de Roode for making useful suggestions on previous versions of the manuscript. The research was supported by NASA Grant NAG5-6101.

APPENDIX A

TKE and Turbulent Fluxes

a. TKE equation

The prognostic equation for TKE e on flux levels is discretized as follows:

$$\frac{e_{n+1}^{j+1/2} - e_n^{j+1/2}}{\delta t} = (P_b^{j+1/2})_{n+1} + (P_s^{j+1/2})_{n+1} - D_{e_{n,n+1}}^{j+1/2} + T_{n+1}^{j+1/2}. \quad \text{(A1)}$$

The subscripts n or $n + 1$ indicate the time step where the terms are computed, while δt is the time increment $t_{n+1} - t_n$. For stability, a backward Euler scheme is used. It is modified to allow a linear tridiagonal implicit solution for the $e^{j+1/2}$ by evaluating at the old time level n those coefficients that multiply each term, e_{n+1}. Resolved-scale TKE advection is neglected.

Production/destruction of TKE by buoyancy forces P_b and shear production P_s are computed as

$$(P_b^{j+1/2})_{n+1} \equiv (\overline{w'b'_{n+1}}^{j+1/2}) = -(K_h)_n^{j+1/2}(N_{n+1}^2)^{j+1/2}, \quad \text{and} \quad \text{(A2)}$$

$$(P_s^{j+1/2})_{n+1} = \rho^{j+1/2} g \left(\overline{w'u'}^{j+1/2}_{n+1} \frac{\delta^{j+1/2}\overline{u}_{n+1}}{\delta p^{j+1/2}} + \overline{w'v'}^{j+1/2}_{n+1} \frac{\delta^{j+1/2}\overline{v}_{n+1}}{\delta p^{j+1/2}} \right), \quad \text{(A3)}$$

where N^2 is the moist buoyancy frequency (*A*12) and K_h is the eddy-diffusivity (10). Dissipation D_e is modeled

$$D_{e_{n,n+1}}^{j+1/2} = \frac{e_{n+1}^{j+1/2}\sqrt{e}_n^{j+1/2}}{l_{\epsilon_n}^{j+1/2}}. \quad \text{(A4)}$$

In (A4), l_ϵ is a length scale for dissipation taken proportional to the turbulent length scale ($l_\epsilon = B_1 l_e$) with $B_1 = 5.87$ (equivalent to MY82 after appropriate translation of notation). Note that for stability, the formulation of the dissipation term is partly implicit. Turbulent transport T_e is parameterized based on downgradient diffusion,

$$T_{n+1}^{j+1/2} = g\rho^{j+1/2}\frac{(\delta^{j+1/2}F_e)_{n+1}}{\delta^{j+1/2}p}, \quad \text{(A5)}$$

where

$$(F_e^j)_{n+1} = g\rho^j K_e^j \frac{\delta^j e_{n+1}}{\delta^j p}. \quad \text{(A6)}$$

As justified in section 6, we use an enhanced eddy viscosity for TKE,

$$K_e^j = \eta_{Te}\sqrt{K_m^{j-1/2}K_m^{j+1/2}}, \tag{A7}$$

with η_{Te} (fixed to 5) a nondimensional coefficient tuned against a variety of convective BL simulations.

We assume no turbulent transport of TKE up through the inversion, so $F_{n+1}^{M+1} = 0$. A boundary condition on e must be specified at the surface pressure level $p_{1/2} = p_s$. Here, TKE is diagnosed according to surface similarity theory and production–dissipation balance (MY82):

$$e_s = B_1^{2/3}u_*^2, \tag{A8}$$

where u_* is the surface friction velocity.

When this scheme was initially implemented, all diffusivities were calculated from TKE, thermodynamic variables, and velocities at time level n. In strongly convective boundary layers at high vertical resolution, this approach produced $2\delta t$ oscillations. These oscillations are due to the very strong dependence of the stability functions (and hence the diffusivities) on the static stability in this regime, which leads to stiffness of the system of prognostic equations. We now use a predictor–corrector approach for calculating the diffusivities that cure this problem at the expense of additional computations. This approach makes the time stepping closer to a fully implicit backward Euler approach: it is more stable and removes the $2\delta t$ oscillations.

b. Computation of N^2

For accurate determination of static stability and buoyancy flux, it is important to evaluate N^2 consistent with moist thermodynamics. Fluctuations in θ_v can be written as

$$\theta_v' = c_t\theta_l' + c_q\theta\frac{L}{C_p}q_t', \tag{A9}$$

where primes denote departures from horizontal average. The dimensionless thermodynamic coefficients c_t and c_q are quite different in locally saturated air than in unsaturated air; in both cases they are weak functions of p and T specified following Cuijpers and Duynkerke (1993). In a layer partly filled with cloud, we use a weighted average of saturated and unsaturated values of c_t and c_q:

$$c_t(\upsilon_s) = \upsilon_s c_t^s + (1 - \upsilon_s)c_t^u, \quad \text{and} \tag{A10}$$

$$c_q(\upsilon_s) = \upsilon_s c_q^s + (1 - \upsilon_s)c_q^u, \tag{A11}$$

where υ_s is the effective saturation fraction. There is some degree of arbitrariness in specifying υ_s. A common approach, used by Ballard et al. (1991), Bechtold et al. (1995), and others, is to specify υ_s to be the cloud fraction at the level of interest; however, this introduces a strong dependence of the PBL model on the host model cloud microphysical scheme. Instead, we suggest that within the context of MY82, $(N^2)^{j+1/2}$ at a given flux level $j + \frac{1}{2}$ is best thought of as a "bulk" buoyancy frequency across the layer from p_j to p_{j+1}. We distinguish two cases. If level $j + 1$ is saturated, we let $\upsilon_s^{j+1/2}$ be the fraction of the layer from p_j to p_{j+1} that is saturated in the horizontal mean (computed using our finite-volume interpretation of the thermodynamic profiles discussed in section a of appendix D). If level $j + 1$ is unsaturated in the mean, we let $\upsilon_s^{j+1/2} = 0$. This case handles the inversion above a stratocumulus layer, and amounts to neglecting the slight warming produced by condensation of liquid water in stratocumulus cloud compared to the generally much larger temperature difference across the inversion. Having specified $\upsilon_s^{j+1/2}$, we define the moist buoyancy frequency at level $j + \frac{1}{2}$ as follows:

$$(N^2)^{j+1/2} = -\rho^{j+1/2}g\frac{g}{\theta_{v,0}}\left[c_t(\upsilon_s^{j+1/2})\frac{\delta^{j+1/2}\theta_l}{\delta^{j+1/2}p} + c_q(\upsilon_s^{j+1/2})\theta^{j+1/2}\frac{L\delta^{j+1/2}q_t}{C_p\delta^{j+1/2}p}\right]. \tag{A12}$$

A corollary to the approximation $\upsilon_s^{M+1/2} = 0$ is that we specify the inversion jump in buoyancy using its unsaturated formula,

$$\Delta_i\theta_v \approx \Delta_i\theta_{vl}, \tag{A13}$$

where $\theta_{vl} \equiv \theta_l(1 + r_m q_t)$ is the liquid water virtual potential temperature and $r_m = 0.608$. Note that θ_{vl} is equal to θ_v in unsaturated air and is conserved in adiabatic displacements of a fluid parcel. This approximation has the attractions of numerical efficiency, and of ready transferability to the restricted inversion entrainment implementation (discussed in section 4c). Because jumps at the top of Sc are large, we have found that this simplification does not alter the model performance.

c. Buoyancy flux at the inversion

Observations and models show that buoyancy fluxes at the top of stratocumulus cloud are often driven by strong longwave radiation cooling, which occurs mainly within 20–100 m of the capping inversion. Coarse mesh models cannot resolve the resulting buoyancy flux profile. This can lead to substantial underestimation of the TKE generation by buoyancy fluxes. We address this problem by assuming that if the PBL is cloud topped and if the thermodynamic level $M + 1$ just above the PBL is unsaturated, all the longwave flux divergence across the uppermost thermodynamic layer containing PBL air is located exactly at the inversion. With the reconstructed inversion, this LW flux divergence is $\delta^{M+1}F_{lw}$ and we can write the buoyancy flux just below the inversion as

$$P_b^i = \frac{g}{\theta_{v,0}}\left[\frac{\delta^{M+1}F_{lw}}{C_p(\rho\Pi)^{M+1}} + \overline{w'\theta_v'}\Big|^i\right], \qquad \text{(A14)}$$

where $\overline{w'\theta_v'}|^i$ is the entrainment flux of θ_v. With the restricted or prognostic inversion, the index M replaces $M + 1$ in the above expression. This enables the TCM to reasonably capture the forcing of convection by cloud-top longwave cooling even at low resolution.

APPENDIX B

Evaporative Enhancement Formulation

As discussed by Randall (1980), the buoyancy of mixtures of cloudy and above-PBL air is piecewise linear in the mixing fraction of above cloud air, with a slope change where the mixture is exactly saturated. Graphically, one can show that

$$E \equiv 1 - \Delta_m b/\Delta_i b = \chi_s(1 - \Delta_i b_s/\Delta_i b). \qquad \text{(B1)}$$

Here, χ_s is the mixing fraction of above-PBL air in an exactly saturated mixture of cloudy and above-PBL air, $\Delta_i b_s = (g/\theta_0)(\beta\Delta_i\theta_e - \theta_0\Delta_i q_t)$, and the thermodynamic parameter β is defined as in Randall (1980). We define Q as $-q_l/\Delta_i q_t$, where q_l is the cloud-top liquid water content. We also define the inversion stability parameter $R \equiv C_p\Pi\Delta\theta_e/(L\Delta q_t)$. We write $\Delta_i b_s$, χ_s, and $\Delta_i b$ in terms of Q and R:

$$\Delta_i b_s = \frac{g}{\theta_0}\frac{L}{C_p\Pi}\Delta q_t(\beta R - \epsilon\Pi), \qquad \text{(B2)}$$

$$\chi_s = \frac{Q}{1 - C_1 R} \quad \text{with } C_1 = \frac{\gamma}{1+\gamma},$$

$$\gamma = \frac{L}{C_p}\frac{\partial q_s}{\partial T}, \quad \text{and} \qquad \text{(B3)}$$

$$\Delta_i b = -\frac{g}{\theta_0}\frac{L\Delta q_t}{C_p\Pi}[-R + k_d - (k_d - \Pi\epsilon)Q], \qquad \text{(B4)}$$

where $k_d = 1 - \Pi\epsilon r_m$ and $\epsilon = C_p\theta_0/L$. Therefore, we have

$$\frac{\Delta_i b_s}{\Delta_i b} = -\frac{\beta R - \Pi\epsilon}{k_d - (k_d - \Pi\epsilon)Q - R}. \qquad \text{(B5)}$$

Now, we eliminate jumps in θ_e in favor of jumps in θ_{vl}. Since

$$\Delta\theta_e = \Delta\theta_{vl} + \frac{L}{C_p}\Delta q_t(\Pi^{-1} - \epsilon r_m), \qquad \text{(B6)}$$

R can be written as

$$R = k_d + \frac{C_p\Pi}{L\Delta q_t}\Delta\theta_{vl}. \qquad \text{(B7)}$$

We introduce the parameters $r = -L\Delta q_t/(C_p\Pi\Delta\theta_{vl})$ and $\lambda = Lq_l/(C_p\Delta\theta_{vl}\Pi)$. Then R and Q can be written in terms of r and λ:

$$R = k_d - \frac{1}{r} \quad \text{and} \quad Q = \frac{\lambda}{r}. \qquad \text{(B8)}$$

Substituting (B8) into (B3) and (B5) gives.

$$\frac{\Delta_i b_s}{\Delta_i b} = \frac{\beta + r(\Pi\epsilon - \beta k_d)}{1 - (k_d - \Pi\epsilon)\lambda} \quad \text{and} \qquad \text{(B9)}$$

$$\chi_s = \frac{\lambda}{C_1 + r(1 - k_d C_1)}. \qquad \text{(B10)}$$

Substituting these expressions into (B1), the evaporative enhancement term can be written

$$E = \lambda F(r, \lambda, p, T), \qquad \text{(B11)}$$

with

$$F(r, \lambda, p, T) = \frac{1 - \beta - (k_d - \Pi\epsilon)\lambda - r(\Pi\epsilon - \beta k_d)}{[1 - (k_d - \Pi\epsilon)\lambda][C_1 + r(1 - k_d C_1)]}. \qquad \text{(B12)}$$

Using typical subtropical parameter values gives values of $F(r, \lambda, p, T)$ around 0.8.

APPENDIX C

Profile Reconstruction

The base of the ambiguous layer (flux level $M + \frac{1}{2}$) is identified as the first flux level above the surface that is saturated, has a Richardson number $\mathrm{Ri}^{M+1/2} > \mathrm{Ri}_c = 0.3$, and is below a minimum PBL top pressure set to 700 mb. If these criteria fail to identify the PBL top (in that case the PBL is not cloud topped), $M + \frac{1}{2}$ is found as the lowest level where $\mathrm{Ri}^{M+1/2} > \mathrm{Ri}_c$. Here, Ri_c is chosen to significantly exceed the maximum gradient Richardson number of 0.19 for a boundary layer in production–dissipation balance permitted by the Galperin et al. (1988) stability functions.

The algorithm described below calculates a unique inversion pressure satisfying the following four conditions once the thermodynamic layer M is found.

1) The inversion lies somewhere in the ambiguous layer, between $p_{M+1/2}$ and $p_{M+3/2}$.
2) Below the inversion, $\theta_{vl} = \theta_{vl}^M$. In the part of the ambiguous layer above the inversion, θ_{vl} is extrapolated downward from its overlying profile.
3) The vertical average of the reconstructed profile of θ_{vl} over the ambiguous layer is θ_{vl}^{M+1}.
4) The inversion jump $\Delta_i\theta_{vl} > \Delta_0$, a threshold value we take as 0.1 K.

First we define a downward-extrapolated θ_{vl} profile. We define $s_{\theta_{vl}}^{M+3/2} = \delta^{M+3/2}\theta_{vl}/\delta^{M+3/2}p$ as the slope of θ_{vl} between p_{M+1} and p_{M+2} and similarly define $s_{\theta_{vl}}^{M+5/2}$. Usually, but not always, $s_{\theta_{vl}}^{M+3/2} < s_{\theta_{vl}}^{M+5/2} < 0$, because the inversion layer is relatively stable. To extrapolate θ_{vl} downward from p_{M+2} to $p_{M+3/2}$, we use $s^+ = \max(s_{\theta_{vl}}^{M+5/2}, s_{\theta_{vl}}^{M+3/2})$. Thus, we define

$$\theta_{vl}^{M+3/2} = \theta_{vl}^{M+2} + s^{+}(p_{M+3/2} - p_{M+2}). \quad \text{(C1)}$$

We then attempt to use this same slope to reconstruct the profile of θ_{vl} down into the ambiguous layer:

$$\theta_{vl}(p) = \begin{cases} \theta_{vl}^{M} & p_{M+1/2} > p > p_i \\ \theta_{vl}^{M+3/2} + s^{+}(p - p_{M+3/2}) & p_i > p > p_{M+3/2}. \end{cases} \quad \text{(C2)}$$

We must choose p_i to produce the correct vertical average of θ_{vl}:

$$\frac{1}{\delta^{M+1}p}\int_{p_{M+1/2}}^{p_{M+3/2}} \theta_{vl}(p)\, dp = \theta_{vl}^{M+1}. \quad \text{(C3)}$$

Let $\mu = (p_{M+3/2} - p_i)/\delta^{M+1}p$ be the above-inversion mass fraction of the ambiguous layer $M + 1$. Substituting (C2) into (C3), we obtain the quadratic equation

$$0 = f(\mu, s^{+}) \equiv -\frac{s^{+}}{2}\delta^{M+1}p\mu^2 + (\theta_{vl}^{M+3/2} - \theta_{vl}^{M})\mu - (\theta_{vl}^{M+1} - \theta_{vl}^{M}). \quad \text{(C4)}$$

The physically meaningful solution with $0 < \mu \leq 1$ can be shown to always be the smaller root of (C4). It is possible for the reconstructed inversion to lie on the flux level $M + \frac{1}{2}$, that is, $\mu = 1$.

Once μ is found, $\Delta_i\theta_{vl}$ can be computed as

$$\Delta_i\theta_{vl} = \theta_{vl}^{M+3/2} - s^{+}\mu\delta^{M+1}p - \theta_{vl}^{M}. \quad \text{(C5)}$$

If this jump is larger than the minimum inversion jump Δ_0, we consider the reconstruction of θ_{vl} by (C2) to be successful and compute the jumps in other variables as explained later. If not, we require that $\Delta_i\theta_{vl} = \Delta_0$. If we knew the inversion height (i.e., μ), the above-inversion slope of θ_{vl} would have to be

$$s^{+}(\mu) = \frac{(\theta_{vl}^{M+3/2} - \theta_{vl}^{M}) - \Delta_0}{\mu\delta^{M+1}p}. \quad \text{(C6)}$$

There is a unique μ for which the resulting reconstructed θ_{vl} profile has the correct vertical average (C3). The equation for μ has the form (C4), but with s^{+} found from (C6). It simplifies to a linear equation with the solution

$$\mu = \frac{2(\theta_{vl}^{M+1} - \theta_{vl}^{M})}{\theta_{vl}^{M+3/2} - \theta_{vl}^{M} + \Delta_0}. \quad \text{(C7)}$$

It can again be shown that $0 < \mu < 1$.

Once p_i is found, the profiles of the conservative variables θ_l, q_t, u, and v in the layer $M + 1$ are found as follows. Let X be any one of these variables. We again assume that $X = X^M$ between $p_{M-1/2}$ and p_i. Since p_i is known, we can deduce the mean value X^{+} of X over the above-inversion fraction of layer $M + 1$ by equating the layer mean of X to X^{M+1}:

$$\mu X^{+} = X^{M+1} - (1 - \mu)X^{M} \quad \text{with}$$

$$X^{+} = \frac{1}{2}(X^{M} + \Delta_i X + X^{M+3/2}). \quad \text{(C8)}$$

With $X^{M+3/2}$ being known from X^{M+2} and $s_X^{M+3/2}$, (C8) is readily solved for the inversion jumps in X.

Note that within this above-inversion layer fraction, we assume that X has a slope equal to the gradient

$$s_X^{+} = \frac{X^{M+3/2} - (X^{M} + \Delta_i X)}{p_{M+3/2} - p_i}. \quad \text{(C9)}$$

Since p_i is not a flux level, we must now use the entrainment fluxes to specify the turbulent energy and water fluxes at the highest flux level $M + \frac{1}{2}$ within the PBL. Between this flux level and the inversion height, the conservative variables have the same values of X^M as in the layer below. Hence the total energy, water, and momentum fluxes vary linearly between $p_{M-1/2}$ and p_i, and they can be linearly interpolated to $p_{M+1/2}$. At p_i, the total energy and water fluxes are

$$E^i = -C_p\Pi^i\rho^{M+1/2}w_e\Delta_i\theta_l + F_r^i, \quad \text{and} \quad \text{(C10)}$$

$$W^i = -\rho^{M+1/2}w_e\Delta_i q_t. \quad \text{(C11)}$$

The fluxes at $p_{M-1/2}$ are computed using turbulence closure and a radiation scheme. Hence,

$$C_p\Pi^{M+1/2}\overline{\rho w'\theta_l'}^{M+1/2} = (1 - \xi)E^{M-1/2} + \xi E^i - F_r^{M+1/2}, \quad \text{(C12)}$$

$$\overline{\rho w' q_t'}^{M+1/2} = (1 - \xi)W^{M-1/2} + \xi W^i - P_{M+1/2}, \quad \text{(C13)}$$

with

$$\xi = \frac{p_{M+1/2} - p_{M-1/2}}{p_i - p_{M-1/2}}. \quad \text{(C14)}$$

If the boundary layer top is saturated, it is assumed that all the radiative flux divergence in the thermodynamic layer containing the inversion occurs within the cloud. Hence

$$F_r^i = F_r^{M+3/2} \quad \text{(C15)}$$

if the PBL is cloud-topped. Reasons for doing this are presented in appendix C of Stevens et al. (1999). Otherwise, the radiative flux at the inversion is computed by linear interpolation between flux levels.

APPENDIX D

Single-Column Model Formulation

In this section, we summarize our single-column model within which we implemented our PBL scheme.

a. Finite-volume interpretation

The model equations are all formulated in terms of fluxes across the boundaries of thermodynamic layers, so it is appropriate to regard the gridpoint values as averages over their thermodynamic layer, a ''finite volume'' interpretation of the equations.

Within layer j, we approximate a prognostic variable X ($=\theta_l$, q_t, u, or v) as

$$X(p) = X^j + s^j\left[p - \frac{1}{2}(p_{j+1/2} + p_{j-1/2})\right]. \quad \text{(D1)}$$

While any specification of the slope s_j will guarantee that the layer average of X will be X_j, we adopt the following specification, which is popular in finite-volume-based advection schemes (Carpenter et al. 1990) because it is second-order accurate and does not create maxima and minima in the profile that are not present in the gridpoint averages. We let

$$s_{j+1/2} = \delta^{j+1/2}X. \quad \text{(D2)}$$

If the slopes $s_{j-1/2}$ and $s_{j+1/2}$ have opposite signs, we take $s_j = 0$. If they have the same sign, we take s_j to be the one of these slopes that has the smaller absolute value. Note that the resulting profile of X will have discontinuities at the flux levels. We also assume that $s_M = 0$, that is, that the layer below the inversion is a mixed layer, a simplification that is quite accurate in practice for a convective PBL in which vertical turbulent mixing minimizes vertical gradients of X. This simplification is useful mainly for a reconstructed inversion; for consistency of presentation we have made it for the other inversion implementations as well.

The treatment of the inversion layer depends on the inversion implementation. With a prognostic inversion, no special treatment is needed. With the reconstructed inversion, inversion reconstruction automatically gives us the desired profiles. If a restricted inversion is used, we assume that the ambiguous layer gridpoint value of any variable uniformly represents the entire ambiguous layer (Fig. 1).

This interpretation of the profiles is used in the single-column model when specification of variables at the flux levels is necessary. For vertical advection, we use (26). At flux levels not adjoining the ambiguous layer, we use the values of $X^{j+1/2}$ from the finite-volume profile for the upwind thermodynamic layer scheme.

b. Statistical cloud model

To determine the mean liquid water content in any layer, we first determine the profiles of q_t and θ_l betwen grid points using our finite-volume reconstruction. Since this profile is well mixed between the highest grid point M within the boundary layer and the inversion pressure p_i, the PBL will be cloud topped if

$$q_{\text{sat}}(T_i, p_i) \leq q_t^M. \quad \text{(D3)}$$

The liquid water at p_i is given by $q_t^M - q_{\text{sat}}(T_i, p_i)$. We calculate the saturation mixing ratio q_s just above and below each flux level and assume (in approximate accordance with our finite volume model) that saturation mixing ratio varies linearly between these points, and (if inversion reconstruction is used) between the highest PBL flux level and the inversion. From the profiles of q_t and q_s, we can deduce the stratocumulus cloud base p_{cb} and the vertically averaged liquid water content within each thermodynamic layer. The cloud base may lie above the highest grid point within the PBL; that is, the PBL may be diagnosed to be cloud topped even if all of the gridpoint values are subsaturated.

To compute cloud–radiation interaction, cloud fraction is estimated using a statistical cloud scheme and assuming a Gaussian probability density function for conserved variables (Bougeault 1981). The saturation deficit variance is estimated as the sum of the variance implied by turbulent moments and a fixed value (taken to be 0.02 times the saturation mixing ratio) linked to fluctuations of conserved variables at the mesoscale.

c. Radiation and surface fluxes

The radiation computations are made using the (NCAR National Center for Atmospheric Research) Community Climate Model 3 (CCM3; Kiehl et al. 1998) radiation code. The cloud emissivity is assumed to be

$$\epsilon = 1 - e^{-1.66\kappa \text{LWP}}, \quad \text{(D4)}$$

where the liquid water path is computed as

$$\text{LWP} = \int_{P_{k+1/2}}^{P_{k-1/2}} \overline{q}_l \frac{dP}{g}. \quad \text{(D5)}$$

In the computation of the cloud optical depth, the effective cloud radius is constant and assumed representative of a warm cloud. It takes the value of 10 μm.

Surface fluxes are also computed as in the NCAR CCM3 GCM (Kiehl et al. 1998), using surface similarity theory.

REFERENCES

Albrecht, B. A., C. S. Bretherton, D. W. Johnson, W. H. Schubert, and A. S. Frisch, 1995: The Atlantic Stratocumulus Transition Experiment—ASTEX. *Bull. Amer. Meteo. Soc.*, **76,** 889–904.

Ayotte, K. W., and Coauthors, 1996: An evaluation of neutral and convective planetary boundary-layer parameterizations relative to large eddy simulations. *Bound.-Layer Meteor.*, **79,** 131–175.

Ballard, S. P., B. W. Golding, and R. N. B. Smith, 1991: Mesoscale model experimental forecasts of the Haar of northeast Scotland. *Mon. Wea. Rev.*, **119,** 2107–2133.

Bechtold, P., J. W. Cuijpers, P. Mascart, and P. Trouilhet, 1995: Modeling of trade wind cumuli with a low order turbulence model: Toward a unified description of Cu and Sc clouds in meteorological models. *J. Atmos. Sci.*, **52,** 455–463.

——, S. K. Krueger, W. S. Lewellen, E. van Meijgaard, H.-C. Hoeng, D. A. Randall, A. van Ulden, and S. Wang, 1996: Modeling a stratocumulus-topped PBL: Intercomparison among different one-dimensional codes and with large eddy simulations. *Bull. Amer. Meteor. Soc.*, **77,** 2033–2042.

Beljaars, A., and P. Viterbo, 1998: Role of the boundary layer in a numerical weather prediction model. *Clear and Cloudy Boundary Layers*, A. A. M. Holtslag and P. G. Duynkerke, Eds., Elsevier, 287–304.

Betts, A. K., 1973: Non-precipitating convection and its parameterization. *Quart. J. Roy. Meteor. Soc.*, **99,** 178–196.

Blackadar, A. K., 1962: The vertical distribution of wind and turbulent

exchange in a neutral atmosphere. *J. Geophys. Res.,* **67,** 3095–3102.

Bougeault, P., 1981: Modeling the trade-wind cumulus boundary layer. Part I: Testing the ensemble cloud relations against numerical data. *J. Atmos. Sci.,* **38,** 455–463.

——, 1985: Diurnal cycle of the marine stratocumulus layer: A higher-order study. *J. Atmos. Sci.,* **42,** 2826–2843.

——, and P. Lacarrère, 1989: Parameterization of orography-induced turbulence in a mesobeta-scale model. *Mon. Wea. Rev.,* **117,** 1872–1890.

Brasseur, O., H. Gallée, G. Schayes, C. Tricot, and K. DeRidder, 1998: Impact of turbulence closures on diurnal temperature evolution for clear sky situations over Belgium. *Bound.-Layer Meteor.,* **87,** 163–193.

Bretherton, C. S., and R. Pincus, 1995: Cloudiness and marine boundary layer dynamics in the ASTEX Lagrangian experiments. Part I: Synoptic setting and vertical structure. *J. Atmos. Sci.,* **52,** 2707–2723.

——, and M. C. Wyant, 1997: Moisture transport, lower tropospheric stability, and decoupling of cloud-topped boundary layers. *J. Atmos. Sci.,* **54,** 148–167.

——, P. Austin, and S. T. Siems, 1995: Cloudiness and marine boundary layer dynamics in the ASTEX Lagrangian experiments. Part II: Cloudiness, drizzle, surface fluxes, and entrainment. *J. Atmos. Sci.,* **52,** 2724–2735.

Carpenter, R. L. J., K. K. Droegemeier, P. R. Woodward, and C. E. Hane, 1990: Application of the Piecewise Parabolic Method (PPM) to meteorological modeling. *Mon. Wea., Rev.,* **118,** 586–612.

Cuijpers, J. M. W., and P. G. Duynkerke, 1993: Large-eddy simulation of trade wind cumulus clouds. *J. Atmos. Sci.,* **50,** 3894–3908.

Deardorff, J. W., 1976: On the entrainment rate of a stratocumulus-capped mixed layer. *Quart. J. Roy. Meteor. Soc.,* **102,** 563–582.

de Roode, S. R., and P. G. Duynkerke, 1997: Observed Lagrangian transition of stratocumulus into cumulus observed during ASTEX: Mean state and turbulence structure. *J. Atmos. Sci.,* **54,** 2157–2173.

Duynkerke, P. G., and P. Hignett, 1993: Simulation of diurnal variation in a stratocumulus-capped marine boundary layer during FIRE. *Mon. Wea. Rev.,* **121,** 3291–3300.

Galperin, B., L. H. Kantha, S. Hassid, and A. Rosati, 1988: A quasi-equilibrium turbulent energy model for geophysical flows. *J. Atmos. Sci.,* **45,** 55–62.

Hignett, P., 1991: Observations of the diurnal variation in a cloud-capped marine boundary layer. *J. Atmos. Sci.,* **48,** 1474–1482.

Kiehl, J. T., J. J. Hack, G. B. Bonan, B. A. Boville, D. L. Williamson, and P. J. Rasch, 1998: The National Center for Atmospheric Research Community Climate Model: CCM3. *J. Climate,* **11,** 1131–1149.

Krueger, S. K., G. T. McLean, and Q. Fu, 1995: Numerical simulations of stratus-to-cumulus transition in the subtropical marine boundary layer. Part I: Boundary layer structure. *J. Atmos. Sci.,* **52,** 2839–2850.

Lenderink, G., and A. A. Holtslag, 2000: Evaluation of kinetic energy approach for modeling turbulent fluxes in stratocumulus. *Mon. Wea. Rev.,* **128,** 244–258.

Lilly, D. K., 1968: Models of cloud-topped mixed layers under a strong inversion. *Quart. J. Roy. Meteor. Soc.,* **94,** 292–309.

Lock, A. P., and M. K. MacVean, 1999: The parameterization of entrainment driven by surface heating and coud-top cooling. *Quart. J. Roy. Meteor. Soc.,* **125,** 271–299.

——, A. R. Brown, M. R. Bush, G. M. Martin, and R. Smith, 2000: A new boundary layer mixing scheme. Part I: Scheme description and single-column model tests. *Mon. Wea. Rev.,* **128,** 3187–3199.

Mellor, G., and T. Yamada, 1982: Development of a turbulence closure model for geophysical fluid problems. *Rev. Astrophys. Space Phys.,* **20,** 851–875.

Moeng, C.-H., and J. C. Wyngaard, 1989: Evaluation of turbulent transport and dissipation closures in second-order modeling. *J. Atmos. Sci.,* **46,** 2311–2330.

——, and P. P. Sullivan, 1994: Comparison of shear and buoyancy driven PBL flows. *J. Atmos. Sci.,* **51,** 999–1022.

——, ——, and B. Stevens, 1999: Including radiative effects in an entrainment rate formula for buoyancy driven PBLs. *J. Atmos. Sci.,* **56,** 1031–1049.

Nicholls, S., 1984: Dynamics of stratocumulus: Aircraft observations and comparisons with a mixed layer model. *Quart. J. Roy. Meteor. Soc.,* **110,** 783–820.

——, and J. Leighton, 1986: Observational study of the structure of stratiform cloud sheets. Part I: Structure. *Quart. J. Roy. Meteor. Soc.,* **112,** 431–460.

——, and J. D. Turton, 1986: Observational study of the structure of stratiform cloud layers. Part II: Entrainment. *Quart. J. Roy. Meteor. Soc.,* **112,** 461–480.

Patankar, S. V., 1980: *Numerical Heat Transfer and Fluid Flow.* Series in Computational Methods in Mechanics and Thermal Sciences, McGraw-Hill, 197 pp.

Randall, D. A., 1976: The interaction of the planetary boundary layer with large-scale circulations. Ph.D. dissertation, University of California, Los Angeles, 247 pp.

——, J. A. Abeles, and T. G. Corsetti, 1985: Seasonal simulations of the planetary boundary layer and boundary layer stratocumulus clouds with a general circulation model. *J. Atmos. Sci.,* **42,** 641–676.

Rogers, D. P., X. Yang, P. M. Norris, D. W. Johnson, G. M. Martin, C. A. Friehe, and B. W. Berger, 1995: Diurnal evolution of the cloud-topped marine boundary layer. Part I: Nocturnal stratocumulus development. *J. Atmos. Sci.,* **52,** 2953–2966.

Stevens, B., 2000: Cloud transitions and decoupling in shear-free stratocumulus topped boundary layers. *Geophys. Res. Lett.,* in press.

——, C.-H. Moeng, and P. P. Sullivan, 1999: Large-eddy simulations of radiatively driven convection: Sensitivities to the representation of small scales. *J. Atmos. Sci.,* **56,** 3963–3984.

Suarez, M. J., A. Arakawa, and D. A. Randall, 1983: Parameterization of the planetary boundary layer in the UCLA general circulation model: Formulation and results. *Mon. Wea. Rev.,* **111,** 2224–2243.

Turner, J. S., 1973: *Buoyancy Effects in Fluids.* Cambridge University Press, 368 pp.

van Zanten., M. C., P. G. Duynkerke, and J. M. W. Cuijpers, 1999: Entrainment parameterization in convective boundary layers derived from large eddy simulations. *J. Atmos. Sci.,* **56,** 813–828.

Wyant, M. C., C. S. Bretherton, H. A. Rand, and D. E. Stevens, 1997: Numerical simulations and a conceptual model of the stratocumulus to trade cumulus transition. *J. Atmos. Sci.,* **54,** 168–192.

Zeman, O., and J. J. Lumley, 1976: Modeling buoyancy driven mixed layers. *J. Atmos. Sci.,* **33,** 1974–1988.